CMS Draft Analysis Note

The content of this note is intended for CMS internal use and distribution only

2010/11/19
Head Id: 8071
Archive Id: 10407:20866M
Archive Date: 2010/06/07
Archive Tag: trunk

Measurement of the B^+ Differential Production Cross Section in pp Collisions at $\sqrt{s} = 7\,\text{TeV}$

D. Lopes Pegna and J. Olsen
Princeton University

Abstract

We present measurements of the B^+ differential production cross sections $d\sigma/dp_T^B$ and $d\sigma/d\left|y^B\right|$ using fully reconstructed $B^+ \to J/\psi K^+$ decays. The J/ψ is reconstructed in the $\mu\mu$ and the cross section is determined in five bins of transverse momentum and five bins of rapidity using a two-dimensional fit to the invariant mass and proper decay length of the B meson. Data are compared to predictions from PYTHIA and MC@NLO.

1 Introduction

The study of heavy-quark production is a key early goal for CMS, both in terms of physics potential and detector commissioning. Even at the lower startup energy of $\sqrt{s} = 7\,\text{TeV}$, the cross section for $b\bar{b}$ production is large enough to provide a few hundred fully reconstructed B^+ decays per pb^{-1}, depending on the desired purity. In addition to providing a check on the CMS mass-scale calibration that is complementary to J/ψ and Υ, the differential cross section measurement provides useful information on next-to-leading order (NLO) QCD calculations in this new energy regime. This note describes the first measurement of the production cross section for fully-reconstructed B mesons at CMS. We use the well-measured decay $B^+ \to J/\psi K^+$, [1] with $J/\psi \to \mu\mu$, for which the product branching fraction is known to a precision of a few percent [1].

1.1 Analysis Strategy

The goal of this analysis is to measure the cross section for the production of B^+ mesons with the smallest amount of understood data necessary to balance the statistical and systematic uncertainties. We exploit the fact that the decay mode has been studied for many years at the Tevatron [2–8] and B Factories [9–11], so that the mass, lifetime, decay dynamics, and polarization are all determined (or known) precisely, and therefore provide sensitive tests of the CMS detector and NLO QCD with very early data. In addition, the dominant background processes from prompt J/ψ and inclusive b production are easily identified and separated from the signal in the data itself using the invariant mass M_B and proper decay length ct of the reconstructed B^+ candidates. [2] The detector signature of residual QCD background from random combinations of decay-in-flight or fake muons with uncorrelated charged particles is also easily separated from the signal decays. We therefore adopt a minimal set of selection criteria in order to maximize the signal efficiency and minimize the integrated luminosity required to perform a first measurement.

After selecting B^+ candidates, the cross section is measured in bins of p_T^B and $\left|y^B\right|$ using a two-dimensional unbinned maximum-likelihood fit. Given that the uncertainty on the luminosity measurement itself is 11% at startup, the goal for this analysis can be quantified as achieving a statistical uncertainty of $\sim 10\%$ on the cross-section measurement in each bin with as little data as possible.

2 Data and Simulation Samples

In Tables 1 and 2 we list the various data and simulated (MC) samples of events used in this version of the note. In processing the data we always use the latest `JSON` file available (currently up through Run 146729) corresponding to $5.8 \pm 0.6\,\text{pb}^{-1}$. The latest MC samples are `Spring2010` and use PYTHIA [12] version 6.416 for simulation of the pp hard scattering. The signal and $b\bar{b}$ background is studied in the inclusive $b \to J/\psi X$ sample, which includes EvtGen [13] for the decay of all b hadrons. The production is split into dedicated samples corresponding to the various b hadron species in order to have a self-calibrating sample whose integrated luminosity can be determined unambiguously. The events are produced with process code `MSEL=1` (minimum bias) and filtered on the presence of at least one b quark (`ID =`

[1] Charge conjugate states are assumed throughout this note.

[2] Throughout this note, the symbol M_B refers to the invariant mass of the reconstructed tracks comprising the B^+ decay, **not** the PDG world-average value.

Table 1: List of data and Monte Carlo samples used in this version of the note.

Process	Dataset
Data Runs 132440–135802	/MinimumBias/Commissioning10-CS_Onia-Jun14thSkim_v1/RAW-RECO
Data Runs 135821–137436	/Mu/Run2010A-CS_Onia-Jun14thSkim_v1/RAW-RECO
Data Runs 138509–140042	/Mu/Run2010A-CS_Onia-v6/RAW-RECO
Data Runs 140042–144114	/MuOnia/Run2010A-PromptReco-v4/RECO
Data Runs 146240–146729	/MuOnia/Run2010B-PromptReco-v2/AOD
$B^+ \to J/\psi X$	/BpToJPsiMuMu_2MuPEtaFilter_7TeV-pythia6-evtgen/Summer10-START36_V9_S09-v1/GEN-SIM-RECO
$B^0 \to J/\psi X$	/B0ToJPsiMuMu_2MuPEtaFilter_7TeV-pythia6-evtgen/Summer10-START36_V9_S09-v1/GEN-SIM-RECO
$B_s \to J/\psi X$	/BsToJPsiMuMu_2MuPEtaFilter_7TeV-pythia6-evtgen/Summer10-START36_V9_S09-v1/GEN-SIM-RECO
$\Lambda_b \to J/\psi X$	/LambdaBToJPsiMuMu_2MuPEtaFilter_7TeV-pythia6-evtgen/Summer10-START36_V9_S09-v1/GEN-SIM-RECO
$pp \to J/\psi X$	/JPsiToMuMu_2MuPEtaFilter_7TeV-pythia6-evtgen/Summer10-START36_V9_S09-v1/GEN-SIM-RECODEBUG
$pp \to \mu\mu X$	/QCD_2MuPEta_7TeV-pythia6-evtgen/Summer10-START36_V10-v1/GEN-SIM-RECO

Table 2: Summary of details for each of the fully simulated samples used in the analysis, including physics process, total number of filtered events $N_{\rm ev}$, pre-filter production cross section σ (including branching fractions for $b \to J/\psi$ and $J/\psi \to \mu\mu$, where appropriate), filter efficiency $\epsilon_{\rm flt}$, and effective integrated luminosity $\mathcal{L}$.

Process	$N_{\rm ev}(10^6)$	σ	$\epsilon_{\rm flt}$	$\mathcal{L}\,({\rm pb}^{-1})$
$B^+ \to J/\psi X$	2.0	30.0μb	0.000932	74
$B^0 \to J/\psi X$	2.2	26.5μb	0.000924	88
$B_s \to J/\psi X$	0.5	24.2μb	0.000314	66
$\Lambda_b \to J/\psi X$	0.5	8.1μb	0.000204	304
$pp \to J/\psi X$	7	12.55μb	0.0433	13
$pp \to \mu\mu X$	26.58	48.44mb	0.00084	0.66

5) in the event. In addition, two muons are required at generator level with $p > 2.5\,{\rm GeV}/c$ and $|\eta| < 2.5$.

2.1 Particle truth matching in simulated events

We use truth matching in this analysis to isolate samples of pure signal decays and separate them from the various types of $b\bar{b}$ backgrounds in the non-prompt J/ψ sample. We do this in order to determine consistently the shapes of the signal and background distributions in M_B and ct, and the associated efficiency for reconstructing true signal decays.

The truth-matching algorithm we use is based on the distance $\Delta R \equiv \sqrt{\Delta\eta^2 + \Delta\phi^2}$ in $\eta - \phi$ space between the reco object and the corresponding generator-level particle. For each reco track we calculate ΔR with respect to every generated charged particle in the event of the same sign, and then select the one with the minimum ΔR. We consider the track to be matched if $\Delta R < 0.02$. Figure 1 shows the distribution of ΔR between the track and the closest generated charged particle for each of the four classes of reco objects in this analysis: muons from J/ψ decay and the kaon in $B^+ \to J/\psi K^+$.

Once the final-state particles (muons, kaons, and pions) are matched to their correct generator-level partners, we then require that the generator-level parent of each muon is a J/ψ. Finally, we require that the parent of the generator-level J/ψ and K is a B^+ meson. In order not to bias the

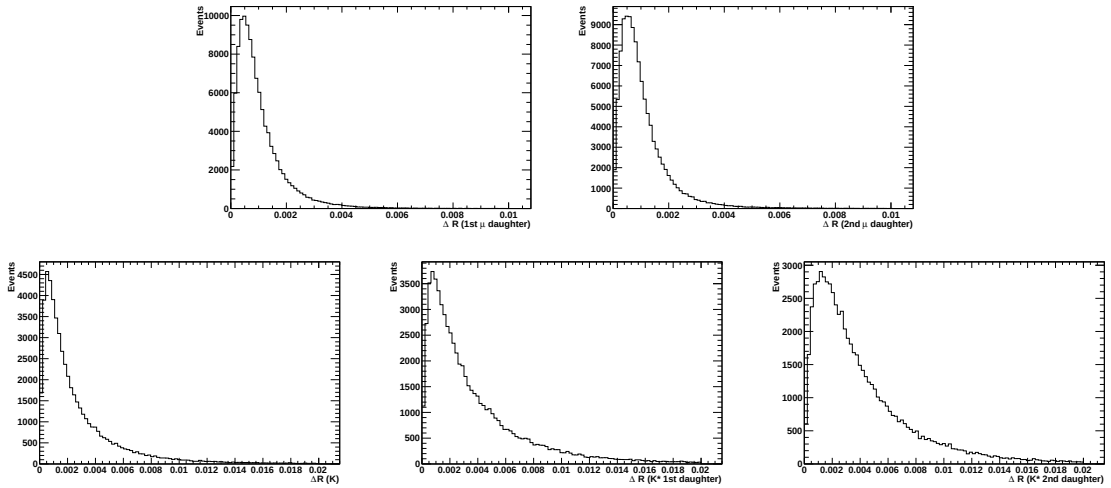

Figure 1: Distributions of the distance ΔR between the reco track and the closest generator-level charged particle for muons from J/ψ decay in $B \to J/\psi K^{(*)}$ (top plots), kaons in $B^+ \to J/\psi K^+$ (bottom right), and kaons (bottom middle) and pions (bottom right) from the K^* in $B^0 \to J/\psi K^{*0}$ decays.

kinematic distributions of the reconstructed B candidates, we do not apply any requirement on the distance between the reconstructed B and its generator-level partner.

3 Event Selection and Reconstruction of B^+ Candidates

Since the goal of this analysis is to measure easily identified exclusive B decays with as little data as possible, for the analysis on the real data we use the available unprescaled muon trigger with the highest efficiency. For the current data used in this version of the note, the trigger line satisfying this criterium is the `HLT_DoubleMu0` trigger. If approved by the ARC and management, we will use the latest data available at the time of approval.

Reconstruction of $B^+ \to J/\psi K^+$ candidates begins by identifying $J/\psi \to \mu\mu$ candidates. We reconstruct J/ψ candidates by vertexing every unique pair of muon objects with opposite electric charge. The vertexing is performed using the Kalman Filter formalism. [3] We require that the vertex fit converges and we select the best J/ψ candidate event-by-event as the one with the mass closest to the world-average value [1]. Figure 2 shows the number of J/ψ candidates in MC before selecting the one with the closest mass. Although this choice biases the dimuon mass distribution in background events, we have confirmed in the prompt and non-prompt J/ψ background samples that the B-mass distribution remains unbiased (see Fig. 11 for distributions of M_B in each of the background categories). This is not surprising, since we constrain the J/ψ mass anyway when vertexing the B candidates.

Both muons comprising the selected J/ψ candidates are required to belong to the `trackerMuon` or `globalMuon` categories and to have fired the trigger. If the muon is in the `globalMuon` category we also require it to be in the `trackerMuon` category. We further require that `trackerMuon` objects pass the arbitration algorithm described in [14]. Reconstruction of `trackerMuon` objects proceeds by associating segments in the muon chambers with a silicon track. However, at reconstruction time a given muon segment can be associated to more than one sili-

[3] As implemented in the `KalmanVertexFitter` class.

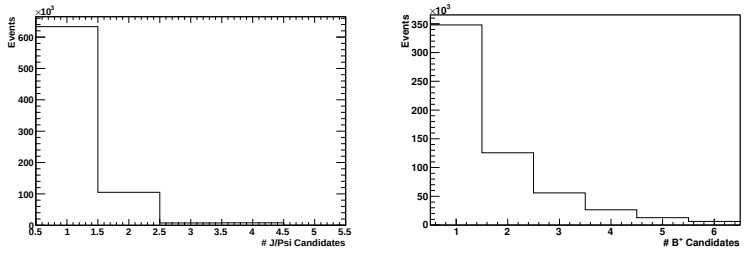

Figure 2: Number of reconstructed J/ψ (left) and B^+ (right) candidates per event after all selection criteria (except the best candidate selection) are applied.

con track, and thus reconstructed `trackerMuons` are allowed to share segments in the muon system. Arbitration is the pattern-recognition process that assigns each segment uniquely to a single `trackerMuon`. The default arbitration algorithm works as follows. Suppose that one segment is associated with more than one `trackerMuon`. For each `trackerMuon` the quantity $\Delta R^2 = \Delta X^2 + \Delta Y^2$ is calculated, where ΔX and ΔY are the distances between the extrapolated silicon track and the segment in local X and Y coordinates. The segment is then uniquely associated to the `trackerMuon` for which ΔR is smallest.

We require the same acceptance criteria as used in the inclusive J/ψ analysis [15]:

- $|\eta^\mu| < 1.3$ and $p_T^\mu > 3.3\,\text{GeV}/c$; or
- $1.3 < |\eta^\mu| < 2.2$ and $p^\mu > 2.9\,\text{GeV}/c$; or
- $2.2 < |\eta^\mu| < 2.4$ and $p_T^\mu > 0.8\,\text{GeV}/c$;

and we retain all J/ψ candidates passing the above selection and having an invariant mass within $150\,\text{MeV}/c^2$ of the nominal value.

Candidate B^+ mesons are reconstructed by combining a J/ψ candidate with a track having $p_T > 0.9\,\text{GeV}/c$, at least three hits, and a track-fit χ^2 less than five times the number of degrees of freedom. We further require that the kaon candidate does not overlap with the muon objects comprising the J/ψ. The p_T threshold on the kaon track was optimized by scanning the value from $500\,\text{MeV}/c$ to $1000\,\text{MeV}/c$ in steps of $100\,\text{MeV}/c$ before choosing one candidate per event, and then comparing the expected statistical uncertainty on the fitted signal yield.

After selection of the kaon track we perform a kinematic fit to the J/ψ – track combination using the method in class `KinematicConstrainedVertexFitter`, where the kaon mass is assigned to the track and the mass of the dimuon pair is constrained to the nominal J/ψ mass. We require that the kinematic fit for each B^+ candidate has a vertex-fit probability greater than 0.001. Figure 2 shows the number of B candidates per event surviving all of the above selection criteria. Due to the large number of multiple candidates per event, we select one unique B^+ candidate per event as the one with the largest value of p_T^B. Finally, we use only selected B candidates in the mass window $4.95 < M_B < 5.55\,\text{GeV}/c^2$ and pseudorapidity range $|\eta^b| < 2.4$. This selection identifies the correct $B^+ \to J/\psi K^+$ candidate 95% of the time in events with a true signal decay at generator level that also have at least one reconstructed B candidate.

3.1 Efficiency from Tag and Probe

We determine the efficiencies of muon reconstruction and selection, muon track reconstruction, and the trigger in bins of p_T and η of the muon using the standard tag-and-probe technique described in detail in Ref. [16, 17], and then applying these efficiencies event-by-event in the signal

Table 3: Muon reconstruction and identification efficiencies measured in data using the tag-and-probe technique on a sample of inclusive J/ψ mesons.

	$\lvert\eta^\mu\rvert$			
p_T^μ (GeV/c)	0.0–0.8	0.8–1.2	1.2–1.6	1.6–2.4
0.0–1.5	0.0	0.0	0.948 ± 0.009	0.955 ± 0.005
1.5–3.0	0.0	0.0	0.958 ± 0.010	0.995 ± 0.003
3.0–4.5	0.994 ± 0.005	0.993 ± 0.007	1.000 ± 0.009	0.993 ± 0.006
4.5–6.0	1.000 ± 0.006	0.994 ± 0.007	1.000 ± 0.009	1.000 ± 0.002
6.0–9.0	1.000 ± 0.010	1.000 ± 0.006	1.000 ± 0.010	1.000 ± 0.005
9.0–20.0	1.000 ± 0.003	0.989 ± 0.020	0.986 ± 0.020	0.999 ± 0.006

MC sample to determine the overal efficiency corresponding to the kinematic distribution of muons from $B^+ \to J/\psi K^+$ decays.

In the tag-and-probe method we use an inclusive J/ψ sample and separate events into in bins of p_T^μ and η^μ for the probe muon. In all cases, the tag muon is a global muon satisfying the cuts listed in the previous section and firing the muon leg of the `MU+TRK` trigger. We then measure three different efficiencies for probe muons:

- **Muon Reco and ID**: here the probe muon is a tracker track with quality cuts, and either matched to a global muon (passing) or not (failing). In Fig. 3 we show the resulting probe-muon identification efficiency as functions of p_T for the entire range $|\eta| < 2.4$, and separately in bins of pseudorapidity, for muons in data and MC. Table 3 summarizes the individual quantitative measurements, and the bin definitions.
- **Muon Tracking**: here the probe muon is a reconstructed segment in the muon chambers matched to a silicon track (passing) or not (failing). Fig. 4 we show the resulting probe muon identification efficiency as functions of p_T for the entire range $|\eta| < 2.4$, and separately in bins of pseudorapidity, for muons in data and MC. Table 4 summarizes the individual quantitative measurements.
- **Trigger**: here the probe muon is a global muon that is also tracker, and satisfies all of the cuts applied to the signal sample. Passing events are those where the tag fires the muon leg of the `Mu+Trk` trigger, and the tag and probe together fire the `DoubleMu0` trigger. Failing events are those that pass only the `Mu+Trk` trigger. Fig. 5 shows the efficiency of a muon to be one leg of the `DoubleMu0` trigger as a function of p_T, and Table 5 summarizes the quantitative results.

Having obtained the efficiencies in bins of muon p_T and η in data, we apply these per-muon efficiencies to muons from B candidates reconstructed in the signal Monte Carlo sample. This calculation is performed by summing the product of weights $w(p_{T1}, \eta_1)$ and $w(p_{T2}, \eta_2)$ for the two muons in each signal decay, where the weight is the product of muon ID, tracking, and trigger efficiencies for a muon with the given values of p_T and η. The total sum, $\sum_i w(p_{T1i}, \eta_{1i}) * w(p_{T2i}, \eta_{2i})$, over all events in a given bin of p_T^B or $\left|y^B\right|$ (η^B) is then the average efficiency of the sample in that bin. Figure 6 shows the reconstruction efficiency as a function of p_T^B and $\left|y^B\right|$, while Table 6 summarizes the efficiency in each bin computed in this way.

We compute the acceptance in MC as the ratio of the number of truth-matched signal decays passing the generator-level filter in a given bin to the number generated in that bin. Table 6 summarizes the acceptance for each bin.

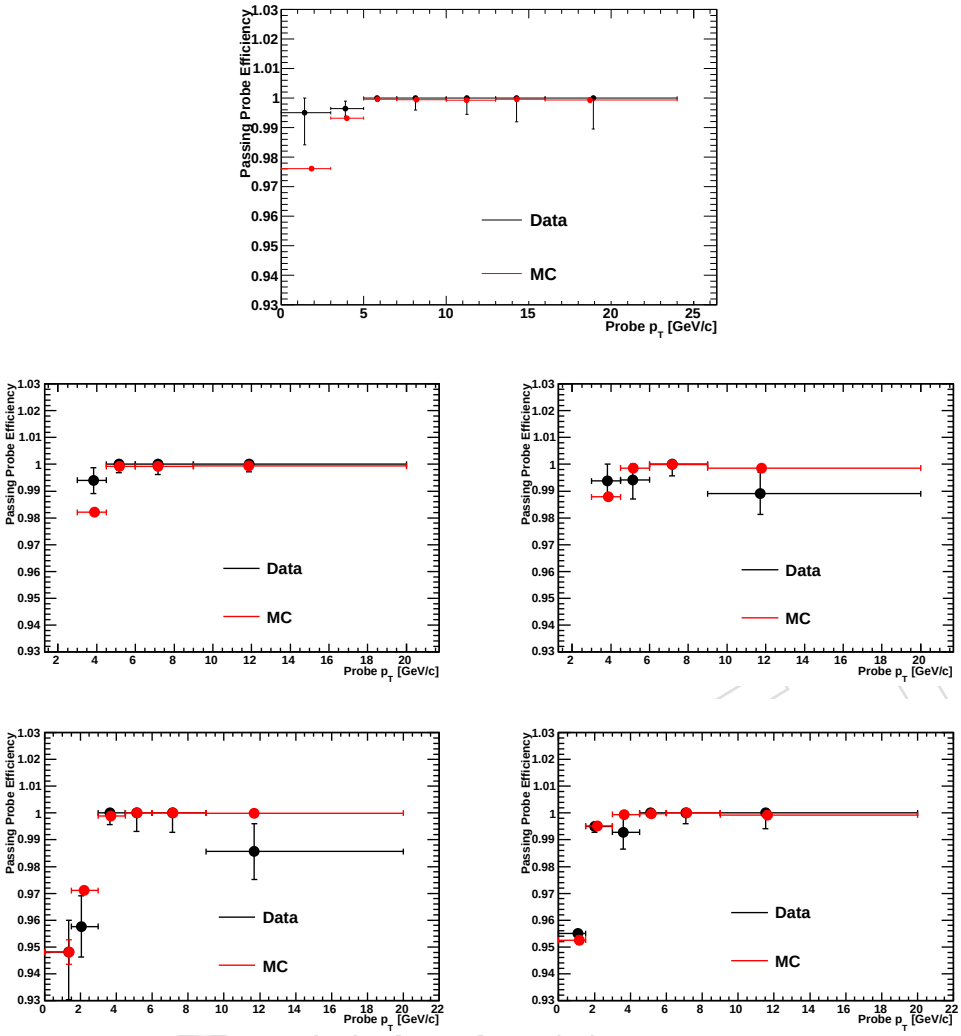

Figure 3: Muon reconstruction and identification efficiency as a function of p_T for $|\eta| < 2.4$ (top), and for several bins in pseudorapidity (clockwise from upper left in second row: $|\eta| < 0.8$, $0.8 < |\eta| < 1.2$, $1.2 < |\eta| < 1.6$, $1.6 < |\eta| < 2.4$), as measured with the tag-and-probe technique on an inclusive J/ψ sample in data. We show data (black points and errors) overlaid on simulation (red points and errors).

Table 4: Muon tracking efficiencies measured in data using the tag-and-probe technique on a sample of inclusive J/ψ mesons.

	$\|\eta^\mu\|$			
p_T^μ (GeV/c)	0.0–0.8	0.8–1.2	1.2–1.6	1.6–2.4
0.0–1.5	0.0	0.0	0.979 ± 0.010	0.987 ± 0.020
1.5–3.0	0.0	0.0	0.996 ± 0.010	0.997 ± 0.007
3.0–4.5	0.999 ± 0.003	1.000 ± 0.006	0.996 ± 0.003	0.996 ± 0.006
4.5–6.0	1.000 ± 0.001	0.998 ± 0.004	1.000 ± 0.010	0.999 ± 0.002
6.0–9.0	0.998 ± 0.002	1.000 ± 0.002	1.000 ± 0.010	0.999 ± 0.010
9.0–20.0	0.998 ± 0.002	0.992 ± 0.008	0.996 ± 0.030	0.993 ± 0.020

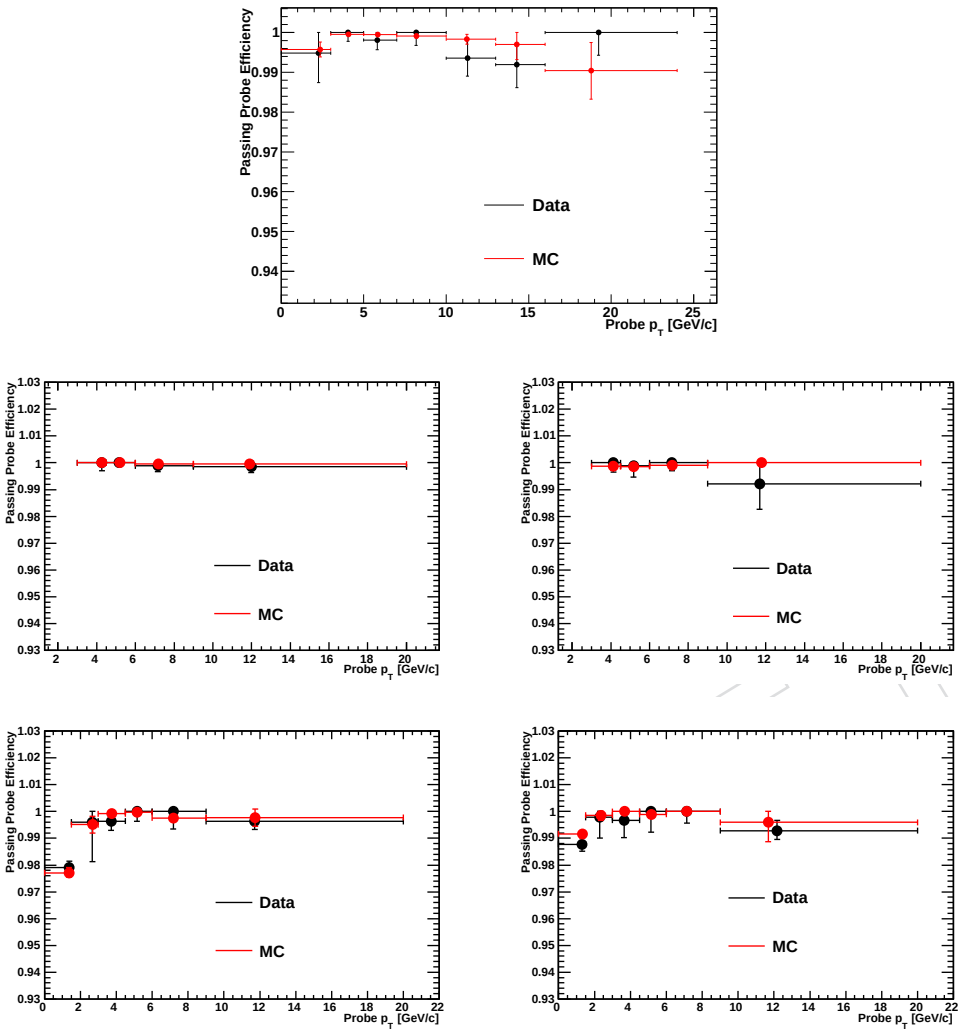

Figure 4: Muon tracking efficiency as a function of p_T for $|\eta| < 2.4$ (top), and for several bins in pseudorapidity (clockwise from upper left in second row: $|\eta| < 0.8$, $0.8 < |\eta| < 1.2$, $1.2 < |\eta| < 1.6$, $1.6 < |\eta| < 2.4$), as measured with the tag-and-probe technique on an inclusive J/ψ sample in data. We show data (black points and errors) overlaid on simulation (red points and errors).

Table 5: Muon trigger efficiency for the `DoubleMu0` trigger measured in data using the tag-and-probe technique on a sample of inclusive J/ψ mesons.

	$\lvert\eta^\mu\rvert$			
p_T^μ (GeV/c)	0.0–0.8	0.8–1.2	1.2–1.6	1.6–2.4
0.0–1.5	0.0	0.0	0.0	0.04 ± 0.05
1.5–3.0	0.0	0.0	0.24 ± 0.04	0.37 ± 0.01
3.0–4.5	0.40 ± 0.01	0.40 ± 0.01	0.78 ± 0.01	0.72 ± 0.01
4.5–6.0	0.77 ± 0.01	0.72 ± 0.01	0.86 ± 0.01	0.75 ± 0.01
6.0–9.0	0.88 ± 0.01	0.84 ± 0.01	0.84 ± 0.02	0.78 ± 0.02
9.0–20.0	0.97 ± 0.01	0.94 ± 0.02	0.91 ± 0.02	0.92 ± 0.02

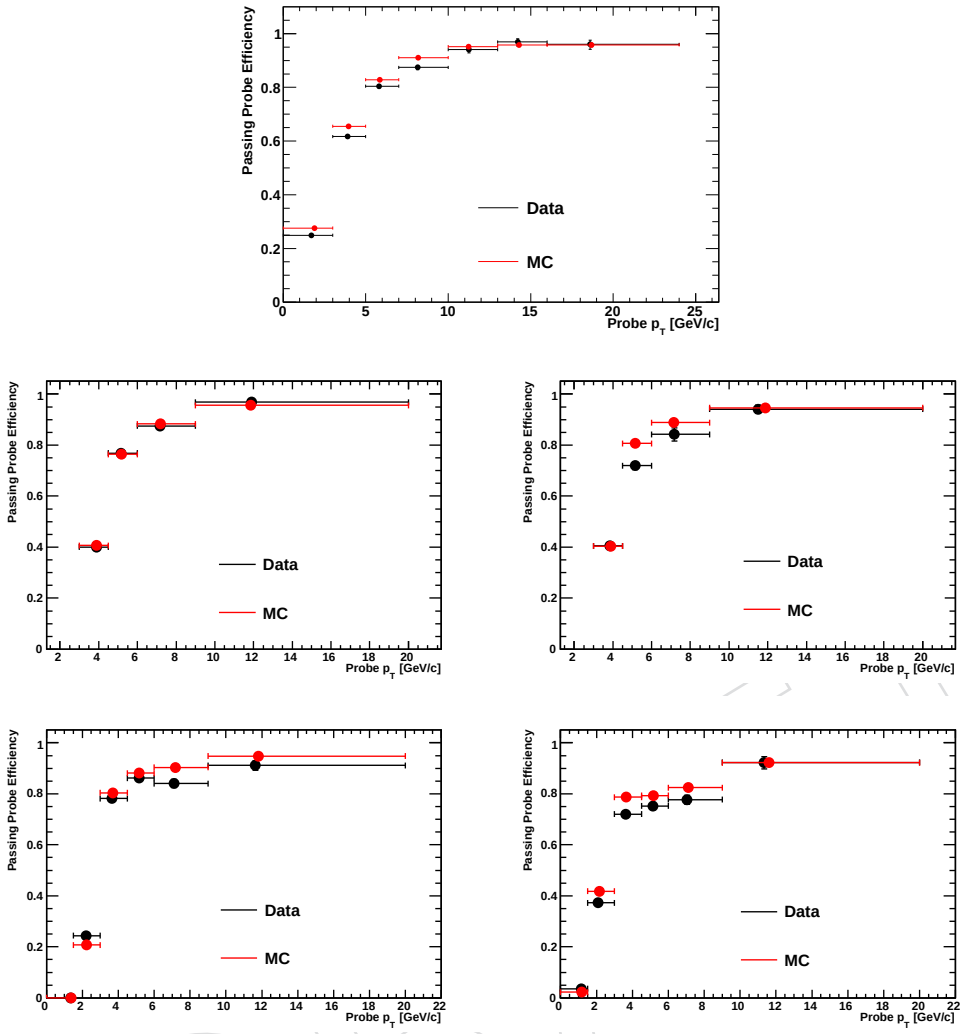

Figure 5: Efficiency of the `DoubleMu0` trigger as a function of p_T for $|\eta| < 2.4$ (top), and for several bins in pseudorapidity (clockwise from upper left in second row: $|\eta| < 0.8$, $0.8 < |\eta| < 1.2$, $1.2 < |\eta| < 1.6$, $1.6 < |\eta| < 2.4$), as measured with the tag-and-probe technique on an inclusive J/ψ sample in data. We show data (black points and errors) overlaid on simulation (red points and errors).

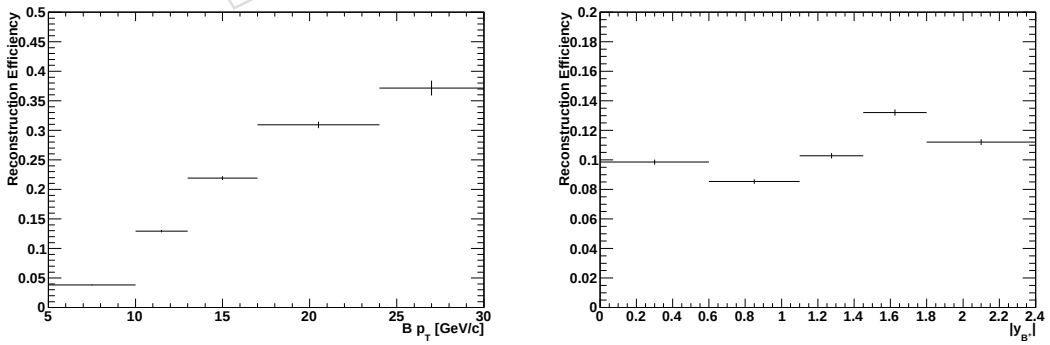

Figure 6: Reconstruction fficiency as a function of p_T^B (left) and $\left|y^B\right|$ (right).

Table 6: Reconstruction efficiency for $B^+ \to J/\psi K^+$ decays computed by applying the efficiencies measured in data to signal MC events, and the acceptance as measured in MC. We report efficiency and acceptance in bins of p_T^B and $|y^B|$.

	Efficiency		Acceptance	
Bin	p_T^B	$\|y^B\|$	p_T^B	$\|y^B\|$
1	0.0381 ± 0.0004	0.0914 ± 0.0016	0.4009 ± 0.0024	0.3290 ± 0.0033
2	0.1292 ± 0.0016	0.0829 ± 0.0015	0.5686 ± 0.0057	0.4595 ± 0.0046
3	0.2190 ± 0.0026	0.1047 ± 0.0019	0.6443 ± 0.0084	0.5652 ± 0.0057
4	0.3092 ± 0.0046	0.1358 ± 0.0020	0.7310 ± 0.0132	0.6066 ± 0.0061
5	0.3717 ± 0.0126	0.1170 ± 0.0020	0.8263 ± 0.0289	0.5389 ± 0.0054
6	0.4092 ± 0.0160	N/A	0.7989 ± 0.0376	N/A

3.2 Proper decay length

The proper decay length ct of the selected B candidates is determined from the measured distance L_{xy} between the primary and B-decay vertices projected on the transverse momentum, and the transverse boost of the reconstructed B meson,

$$ct = \frac{M_B}{p_T^B} L_{xy}, \tag{1}$$

where M_B and p_T^B are the mass and transverse momentum of the B candidate, respectively. The transverse flight length L_{xy} is the projection of the vector $\vec{s}$ pointing from the primary to the secondary vertex onto the transverse momentum,

$$L_{xy} = \frac{\vec{s} \cdot \vec{p}_T^B}{|\vec{p}_T^B|}. \tag{2}$$

To calculate the primary vertex we use the code described in Ref. [18], where in the case of multiple vertices we choose the one with the best probability.

The ct residuals for truth-matched signal and $pp \to J/\psi$ events, computed as $ct(\text{reco}) - ct(\text{true})$, are shown in Fig. 7, while scatter plots of ct vs. reconstructed p_T and η of B^+ candidates are shown in Fig. 8. The rms of the ct residual distribution is approximately 40 μm for correctly reconstructed B^+ decays, while it is significantly worse (> 50 μm) for misreconstructed events including a real prompt J/ψ.

4 Sample Composition

Figure 9 shows the fraction of truth-matched signal events coming from the various PYTHIA production processes: leading order (flavor creation), and the two next-to-leading-order (NLO) processes (flavor excitation and gluon splitting). The events arise predominantly from the flavor-excitation process, with only about 20% of events arising from leading-order production. Thus, the differential cross section measurement in these modes is directly sensitive to the NLO contribution, and serves as a first check on the theory prediction in this new energy regime.

We use generator-level information to identify five general sources of background events in the samples listed in Table 1:

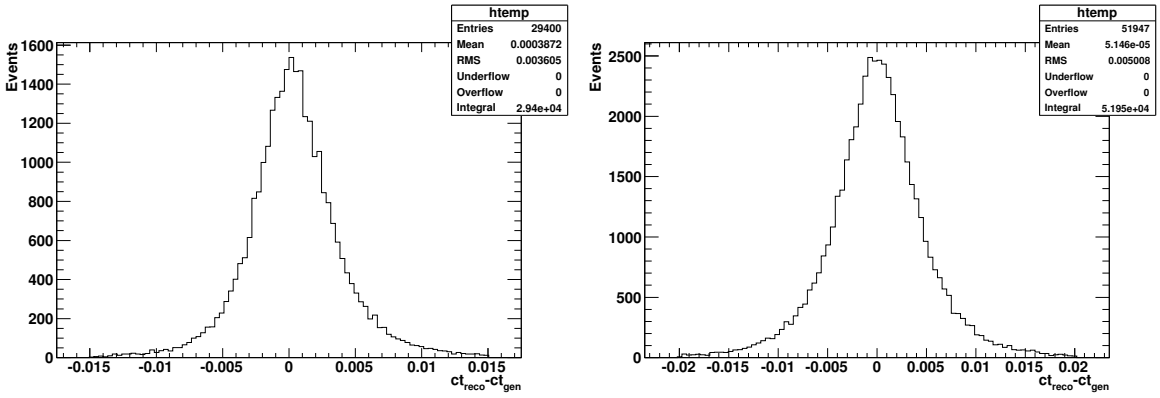

Figure 7: Distributions of $ct(\text{reco}) - ct(\text{true})$ for truth-matched B^+ candidates passing all selection criteria in the $b \to J/\psi X$ (left) and $pp \to J/\psi X$ (right) samples.

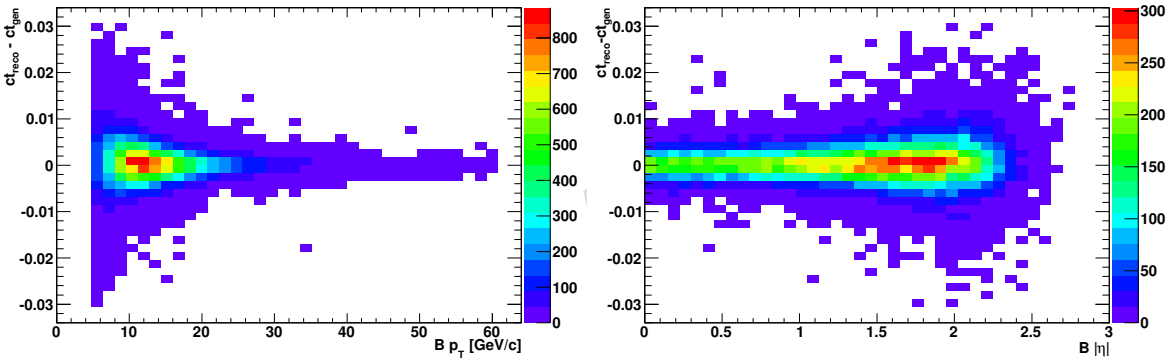

Figure 8: Scatter plots of $ct(\text{reco}) - ct(\text{true})$ vs. p_T^B (left) and η^B (right) for truth-matched B^+ (left) candidates passing all selection criteria.

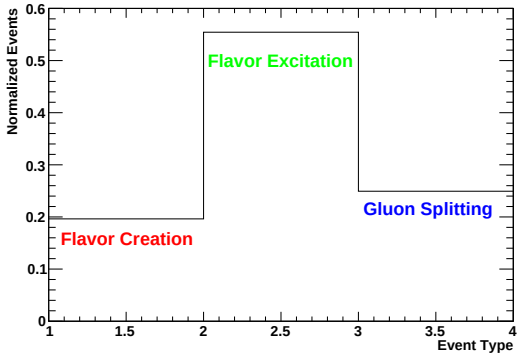

Figure 9: Breakdown of production fractions for the various processes contributing to exclusive $B^+ \to J/\psi K^+$ (left) events passing all selection criteria in the $b \to J/\psi X$ sample.

- $B \to J/\psi\pi$ – Cabibbo-suppressed analog of the the $B^+ \to J/\psi K^+$ decay. The fraction of this mode relative to the Cabibbo-allowed mode scales like $|V_{cd}/V_{cs}|^2 \sim 5\%$ and has been measured with a relative precision better than 10% [11]. We include this component as a fixed fraction of the signal in the fit, and vary it as a systematic uncertainty.
- **Peaking** B – Dominated by $B^0 \to J/\psi K^{*0}$ events where the pion from the K^* decay is lost, and $B \to \chi_c X$ decays where the χ_c decays to J/ψ and a random track is added. We have searched for a specific component of peaking background events from $\Lambda_b \to J/\psi X$ events, but find only a smooth distribution in M_B from truth-matched events (see Fig. 10). We therefore do not include an explicit peaking component for this process in the nominal fit.
- **Non-prompt** J/ψ – pure combinatorial background from $b\bar{b}$ events that contain a real J/ψ at generator level, but do not peak in the B mass. This component is dominated by a non-prompt contribution from misreconstructed b-hadron decays, but also includes a non-negligible contribution from "prompt-like" events that peak at zero lifetime. These prompt events have been investigated at the generator level and arise from combinations of J/ψ and a random track that produce an average vertex near the primary, thus giving $ct \sim 0$.
- **Prompt** J/ψ – true $pp \to J/\psi$ with added tracks to make $B^+ \to J/\psi K^+$ candidates. This background is the least correlated with the signal because it is smoothly varying in M_B and isolated near $ct \sim 0$. It is therefore easily separated in the fit and has little impact on the signal-yield uncertainty.
- **"QCD" Background** – all other backgrounds that include at least one true muon at generator level. This includes $b\bar{b}$, $c\bar{c}$, and gluon/light-quark events with muons from decays in flight of π and K mesons. The effective integrated luminosity of the `ppMuX` sample is not sufficient to accurately estimate either the size or distributions of these events. However, we use the sideband of the dimuon mass distribution before selecting the best J/ψ candidate using the mass to determine that the contribution from fake J/ψ in events not continaing a real b hadron is negligible.

5 Fitting Procedure

We extract signal yields in each p_T^B and y^B bin, where

$$y^B = \frac{1}{2}\ln\left(\frac{E^B + p_z^B}{E^B - p_z^B}\right), \tag{3}$$

using a data-driven unbinned extended maximum-likelihood fit to the invariant mass M_B and proper decay length ct of the reconstructed candidates. The likelihood for event j is obtained by summing the product of yield n_i and probability density $\mathcal{P}_i$ for each of the signal and background hypotheses i assumed to be in the sample. We assume the existence of five separate components ($i = 1,5$): signal, $B^+ \to J/\psi\pi^+$ (fixed), prompt J/ψ, non-prompt J/ψ, and $b\bar{b}$ events that peak in M_B. The extended likelihood function is then the product of likelihoods for each event j:

$$\mathcal{L} = \exp\left(-\sum_i n_i\right)\prod_j\left[\sum_i n_i \mathcal{P}_i(M_B;\vec{\alpha}_i)\mathcal{P}_i(ct;\vec{\beta}_i)\right]. \tag{4}$$

The probabilities $\mathcal{P}_i$ are the probability density functions (PDFs) with shape parameters $\vec{\alpha}_i$ for M_B and $\vec{\beta}_i$ for ct, evaluated separately for each of the i fit components. The yields n_i are then de-

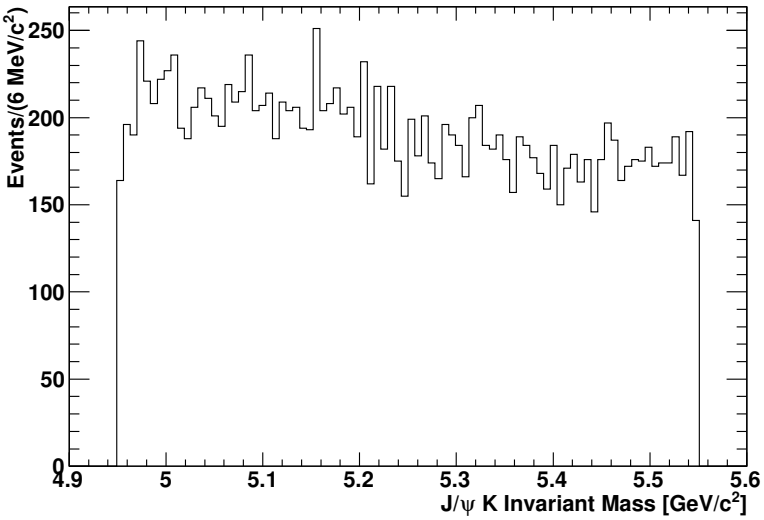

Figure 10: Distribution of reconstructed M_B for background events truth-matched as having come from the decay $\Lambda_b \to J/\psi X$.

Table 7: Bin definitions for p_T^B, y^B, and η^B.

Bin #	p_T^B (GeV/c)	$\lvert y^B \rvert$	η^B
1	$(5, 10)$	$(0.00, 0.60)$	$(-2.4, -1.6)$
2	$(10, 13)$	$(0.60, 1.10)$	$(-1.6, -0.7)$
3	$(13, 17)$	$(1.10, 1.45)$	$(-0.7, +0.7)$
4	$(17, 24)$	$(1.45, 1.80)$	$(+0.7, +1.6)$
5	$(24, 30)$	$(1.80, 2.40)$	$(+1.6, +2.4)$
6	> 30	N/A	N/A

termined by maximizing the quantity $\ln \mathcal{L}$ while keeping the PDF parameters ($\vec{\alpha}_i$ and $\vec{\beta}_i$) fixed. As a cross check, we also perform a measurement of $d\sigma/d\eta^B$ (ie, not applying the absolute value) in order to show the forward/backward symmetry of the measurement. Table 7 shows the definition of bin edges for p_T^B, y^B, and η^B, where we use a constant value of $p_T^B = 5\,\text{GeV}/c$ in the definition of rapidity.

5.1 Probability density functions

The PDFs are constructed from common functions (Gaussian, exponential, etc) and the parameters are initially determined from the MC samples. The guiding principle we follow in designing the PDFs is to use the simplest function with the least number of parameters necessary to adequately describe the observed distribution of events in M_B and ct for each component. We determine systematic uncertainties on yields due to our (potentially) incomplete knowledge of the true distributions by varying the PDF parameters within their uncertainties (see Sec. 7).

Table 8 lists the functional forms used to define the PDFs. Figures 11 and 12 show the fit results for the M_B and ct PDFs for each component, as obtained from the available MC samples, which is the starting point for the data-driven technique described in the next section. For M_B, we use the sum of three Gaussians to describe the signal shape, and two Gaussians to describe the

Table 8: Summary of generic M_B and ct PDFs used in the fit. The common ct resolution function $\mathcal{R}$ is defined as the sum of three Gaussian functions for the two lowest p_T^B bins, and three Gaussians for the two highest bins. For y^B and η^B we use two Gaussians for the central (barrel) region, and three Gaussians for the forward/backward regions. In the case of $J/\psi\pi$ we use the same ct parameters as the signal.

Component	M_B	ct
Signal	$G_{\text{core}} + G_{\text{tail}} + G_{\text{out}}$	$\mathcal{R} \otimes e^{-ct/\tau_B}$
$J/\psi\pi$	$G_{\text{core}} + G_{\text{out}}$	$\mathcal{R} \otimes e^{-ct/\tau_B}$
Peaking B	$G_1 + G_2 + e^{-\alpha M_B}$	$\mathcal{R} \otimes e^{-ct/\tau_{\text{MC}}}$
non-prompt J/ψ	$e^{-\alpha M_B}$	$\mathcal{R} \otimes (e^{-ct/\tau_1} + e^{-ct/\tau_2})$
Prompt J/ψ	$e^{-\alpha M_B}$	$\mathcal{R}\otimes$

$J/\psi\pi$ shape. We use exponentials for the prompt J/ψ and combinatorial $b\bar{b}$ components, and a combination of two Gaussians and an exponential to describe the peaking background component. For ct, every component shares the same resolution function $\mathcal{R}$, which is taken to be the sum of three Gaussians for the two lowest p_T^B bins, and two Gaussians for the three highest p_T^B bins. For the fits in bins of $|y^B|$ we use two Gaussians for the first two (barrel) bins, and three Gaussians for the three outer bins. For η^B we use two Gaussians for the three barrel bins, and three Gaussians for the two forward/backward bins. For signal (and $J/\psi\pi$), we convolve the resolution function with a single exponential with the PDG B^+ lifetime. For combinatorial and peaking $b\bar{b}$ components we convolve $\mathcal{R}$ with the sum of two exponentials that represent the average lifetime in these samples of misreconstructed b-hadron decays. Finally, for the prompt J/ψ component we use the pure resolution function $\mathcal{R}$.

Since we form the probabilities for each component to be the product of PDFs for M_B and ct, we are implicitly assuming that these two variables are uncorrelated. Any correlation between them in either the signal or background components could cause a bias in the fitted yields. To check this we plot in Figs. 13 and 14 correlation and profile plots of M_B vs. ct for each of the components in the fit. No significant correlations are observed. We also calculate the linear correlation coefficients between each pair of variables for all of the components and find that they are all 2% or less.

5.2 Data-driven Procedure to Determine PDF Parameters

The analysis proceeds in several steps that allow us to obtain all background shapes, apart from the peaking $b\bar{b}$ component, directly from data. This data-driven technique relies on the assumption that above the signal peak in M_B there are only two contributions: prompt J/ψ and combinatorial $b\bar{b}$ background. This allows us to extract simultaneously the ct resolution function parameters (from the prompt J/ψ events), and the lifetime parameters describing the non-prompt background from $b\bar{b}$ events. Simulation indicates that the lifetime parameters of the non-prompt background are approximately independent of p_T^B, so we fit for them using the full sample with $p_T^B > 5\,\text{GeV}/c$ in the upper mass sideband, and then fix them in all subsequent fits in bins of p_T^B, $|y^B|$, and η^B. The resolution function parameters are then determined bin-by-bin fitting the upper mass sideband in data.

The fit proceeds in three steps, where the first step uses the shape parameters obtained from MC (Figs. 11 and 12) as the starting point:

Step 1 – Fit ct for events in the high-mass sideband region $M_B > 5.4\,\text{GeV}/c^2$ for all

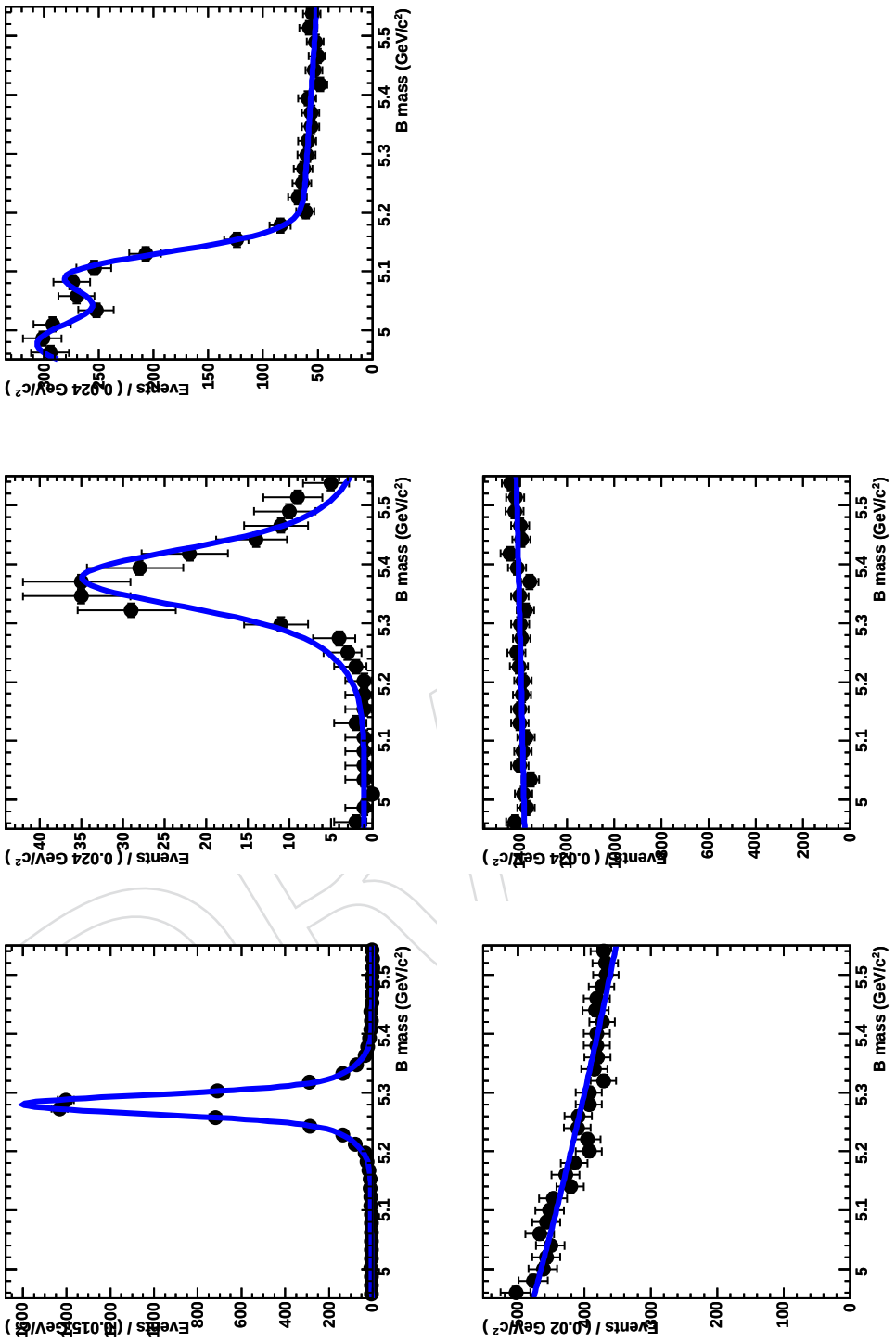

Figure 11: Fits to determine PDF parameters for M_B in the sample of $B^+ \to J/\psi K^+$ events corresponding to (from upper left to lower right): signal, $J/\psi\pi$, peaking $b\bar{b}$, non-prompt J/ψ, and prompt J/ψ.

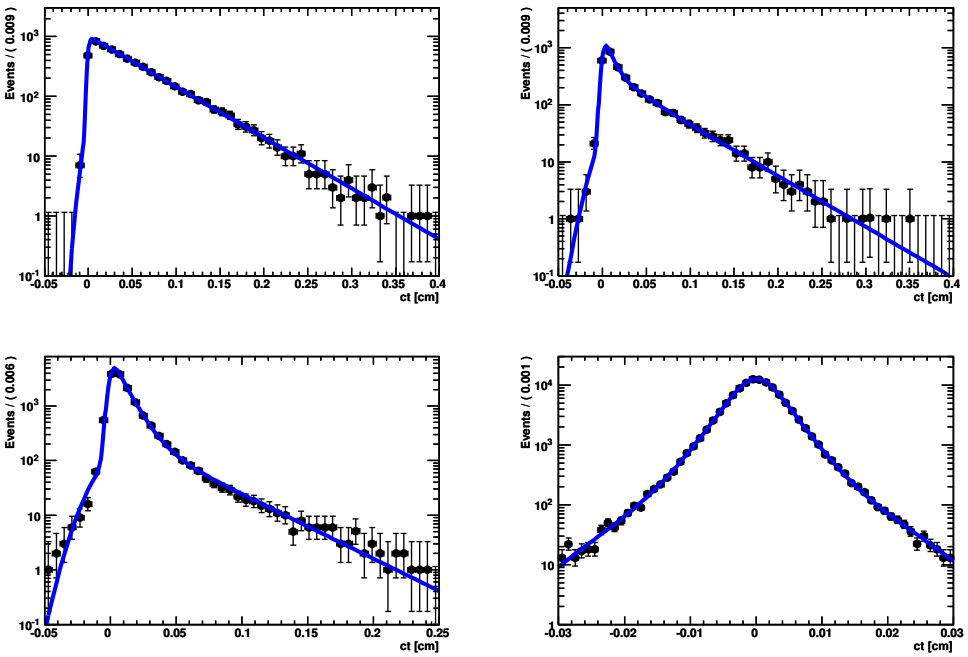

Figure 12: Fits to determine PDF parameters for ct in the sample of $B^+ \to J/\psi K^+$ events corresponding to (from upper left to lower right): signal, peaking $b\bar{b}$, non-prompt J/ψ, and prompt J/ψ. The ct PDF parameters for $B^+ \to J/\psi\pi^+$ events are the same as those of the signal events.

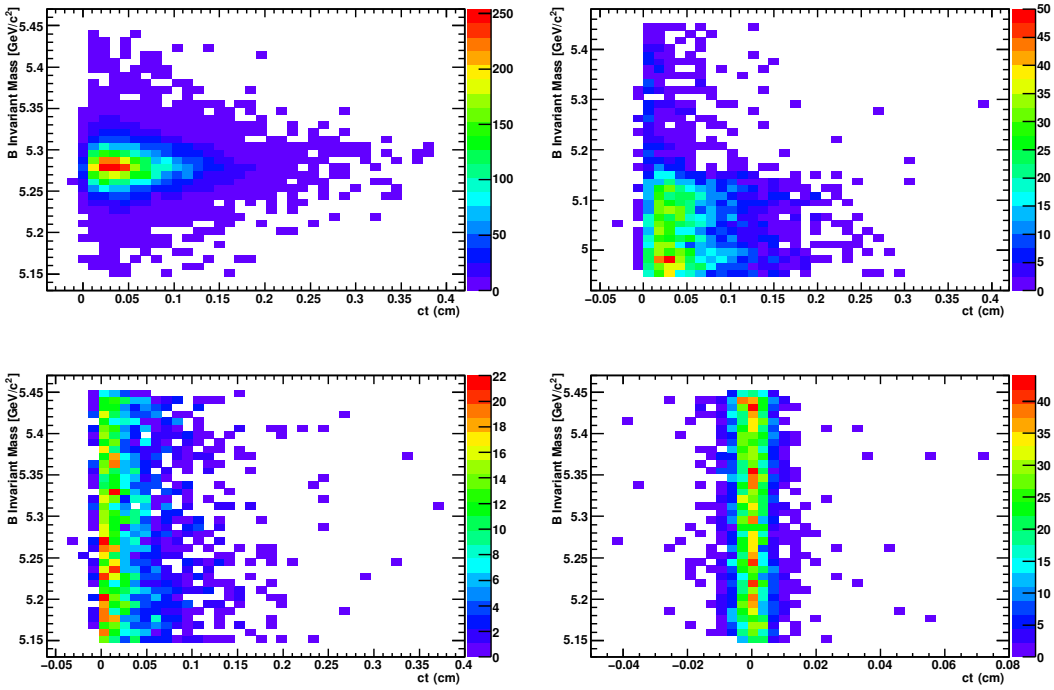

Figure 13: Scatter plots of M_B vs. ct for B^+ candidates corresponding to (from upper left to lower right): signal, peaking $b\bar{b}$, non-prompt J/ψ, and prompt J/ψ.

Table 9: Summary of the background ct parameters determined by fitting the upper M_B sideband in data for different bins in p_T^B. We use the parameters determined in bin 4 to describe the resolution function and background lifetime in bins 5 and 6.

Parameter	$p_T^B > 5\,\text{GeV}/c$	Bin 1	Bin 2	Bin 3	Bin 4
f_{core}	0.551 ± 0.051	0.536 ± 0.076	0.733 ± 0.059	0.814 ± 0.058	0.941 ± 0.033
f_{tail}	0.398 ± 0.045	0.400 ± 0.061	0.259 ± 0.011	0.186 ± 0.058	0.059 ± 0.033
f_{prompt}	0.842 ± 0.021	0.776 ± 0.018	0.737 ± 0.027	0.632 ± 0.044	0.689 ± 0.057
$\sigma_{\text{core}}\,(\mu\text{m})$	30.8 ± 1.5	36.7 ± 2.8	29.2 ± 1.6	26.3 ± 1.8	22.8 ± 1.7
$\sigma_{\text{tail}}\,(\mu\text{m})$	73.0 ± 5.1	86.3 ± 9.4	69.8 ± 6.9	76.8 ± 11.5	126 ± 42
$\sigma_{\text{out}}\,(\mu\text{m})$	208 ± 22	215 ± 30	175 ± 83	N/A	N/A
$c\tau_1\,(\mu\text{m})$	72.9 ± 1.5	fixed	fixed	fixed	fixed
$c\tau_2\,(\mu\text{m})$	460 ± 5	fixed	fixed	fixed	fixed

candidates with $p_T^B > 5\,\text{GeV}/c$, $|y^B| < 2.4$, and $|\eta^B| < 2.4$ assuming two components (prompt and non-prompt J/ψ) to obtain the parameters describing the lifetime of the combinatorial $b\bar{b}$ background (2 lifetime parameters). In this fit we also allow the resolution function, which is the same for the prompt and non-prompt components, to vary freely;

Step 2 – Fix the lifetime parameters obtained in `Step 1` and then fit ct in the upper mass sideband separately in each bin of p_T^B, $|y^B|$, and η^B to obtain the p_T- and y^B (η)-dependent resolution function parameters. We find that the resolution function requires three separate Gaussians for the two lowest p_T bins, while two Gaussians is sufficient for the three highest p_T bins. For η^B, three Gaussian functions are used for the resolution function in the forward/backward bins, while two Gaussians is sufficient to describe the resolution function in the barrel. Since there is very little background in the two highest p_T bins, we use the parameters determined in the third highest bin also for those bins;

Step 3 – Fixing all ct PDF parameters that were determined in `Steps 1` and `2`, perform the final fit in the entire mass range, including the signal region, to obtain the signal yield in each bin of p_T^B. The only floating parameters in this fit are the yields for each individual component, and the M_B shapes of the prompt and combinatorial backgrounds (one parameter for each component). We use the signal M_B shape determined from MC, including the official momentum-scale correction applied to the measured mass in data, and we use the PDG value for the average B^+ lifetime. For the peaking background we use the ct and M_B shape parameters determined from MC; only the yield is allowed to vary.

Tables 9- 11 summarize the various parameters determined in each of the ct fits in the upper M_B sideband, while Figs. 15 and 16 show the results compared to data for all fits.

5.3 Fit Validation

For a detailed set of fit validations, please see the internal documentation for the previous analysis [19]. All of the studies performed previously are still relevant to the current analysis, but for brevity we have chosen not to reproduce them here.

To demonstrate that our nominal fit configuration is inherently unbiased, we show in Figs. 17–19 the resulting pull distributions in all bins of p_T^B for 400 toy experiments corresponding to the

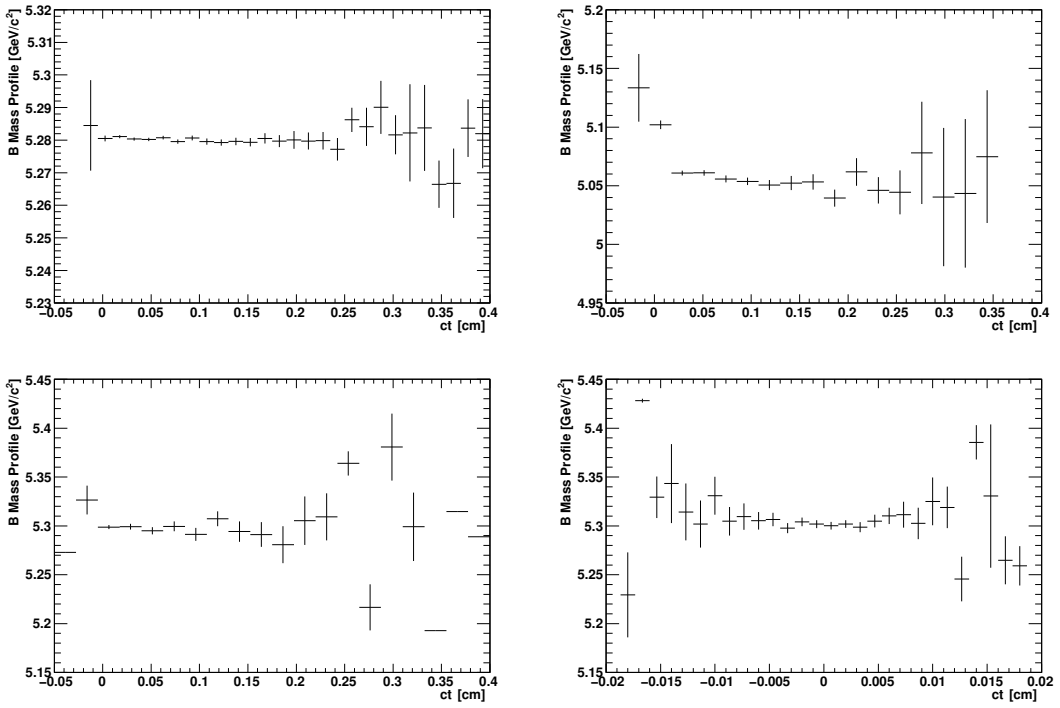

Figure 14: Profile plots of M_B vs. ct for B^+ candidates corresponding to (from upper left to lower right): signal, peaking $b\bar{b}$, non-prompt J/ψ, and prompt J/ψ.

Table 10: Summary of the background ct parameters determined by fitting the upper M_B sideband in data for different bins in $|y^B|$.

Parameter	Bin 1	Bin 2	Bin 3	Bin 4	Bin 5
f_{core}	0.694 ± 0.082	0.685 ± 0.080	0.714 ± 0.057	0.392 ± 0.119	0.309 ± 0.126
f_{tail}	0.306 ± 0.082	0.315 ± 0.080	0.258 ± 0.054	0.557 ± 0.109	0.568 ± 0.097
f_{prompt}	0.831 ± 0.022	0.848 ± 0.019	0.864 ± 0.019	0.834 ± 0.018	0.841 ± 0.019
$\sigma_{\text{core}}\,(\mu\text{m})$	27.1 ± 2.5	28.5 ± 2.2	33.9 ± 1.8	29.3 ± 4.6	28.1 ± 6.2
$\sigma_{\text{tail}}\,(\mu\text{m})$	49.8 ± 7.6	67.6 ± 7.2	84.1 ± 9.1	67.7 ± 6.9	70.2 ± 10.7
$\sigma_{\text{out}}\,(\mu\text{m})$	N/A	N/A	283 ± 69	211 ± 36	194 ± 27
$c\tau_1\,(\mu\text{m})$	fixed	fixed	fixed	fixed	fixed
$c\tau_2\,(\mu\text{m})$	fixed	fixed	fixed	fixed	fixed

Table 11: Summary of the background ct parameters determined by fitting the upper M_B sideband in data for different bins in η^B.

Parameter	Bin 1	Bin 2	Bin 3	Bin 4	Bin 5
f_{core}	0.304 ± 0.086	0.860 ± 0.040	0.722 ± 0.113	0.822 ± 0.039	0.454 ± 0.095
f_{tail}	0.630 ± 0.077	0.140 ± 0.005	0.278 ± 0.043	0.178 ± 0.008	0.436 ± 0.091
f_{prompt}	0.808 ± 0.020	0.814 ± 0.020	0.828 ± 0.022	0.864 ± 0.019	0.891 ± 0.017
$\sigma_{\text{core}}\,(\mu\text{m})$	26.9 ± 4.2	35.4 ± 1.8	26.5 ± 2.2	33.7 ± 1.6	32.4 ± 3.7
$\sigma_{\text{tail}}\,(\mu\text{m})$	68.0 ± 5.7	106 ± 13	55.8 ± 7.5	101 ± 11	74.9 ± 9.3
$\sigma_{\text{out}}\,(\mu\text{m})$	237 ± 37	N/A	N/A	N/A	174 ± 23.6
$c\tau_1\,(\mu\text{m})$	fixed	fixed	fixed	fixed	fixed
$c\tau_2\,(\mu\text{m})$	fixed	fixed	fixed	fixed	fixed

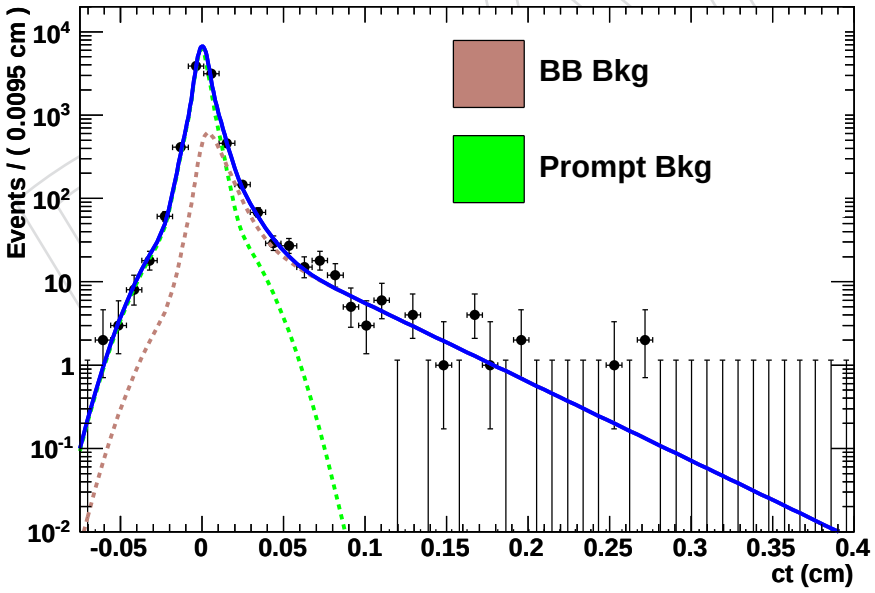

Figure 15: Results of fitting ct in the upper sideband of M_B for events with $p_T^B > 5\,\text{GeV}/c$ in order to determine the lifetime parameters for the non-prompt J/ψ background.

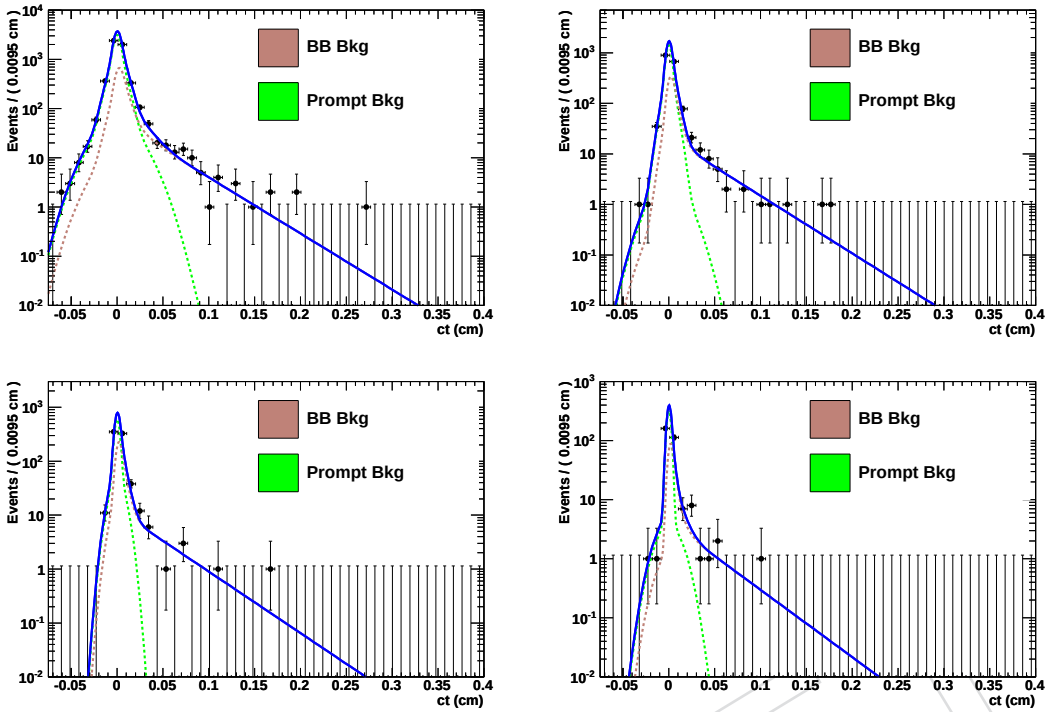

Figure 16: Results of fitting ct in the upper sideband of M_B for events in the first four bins of p_T^B (increasing clockwise from top left to bottom right) in order to determine the parameters of $\mathcal{R}$ separately in each bin.

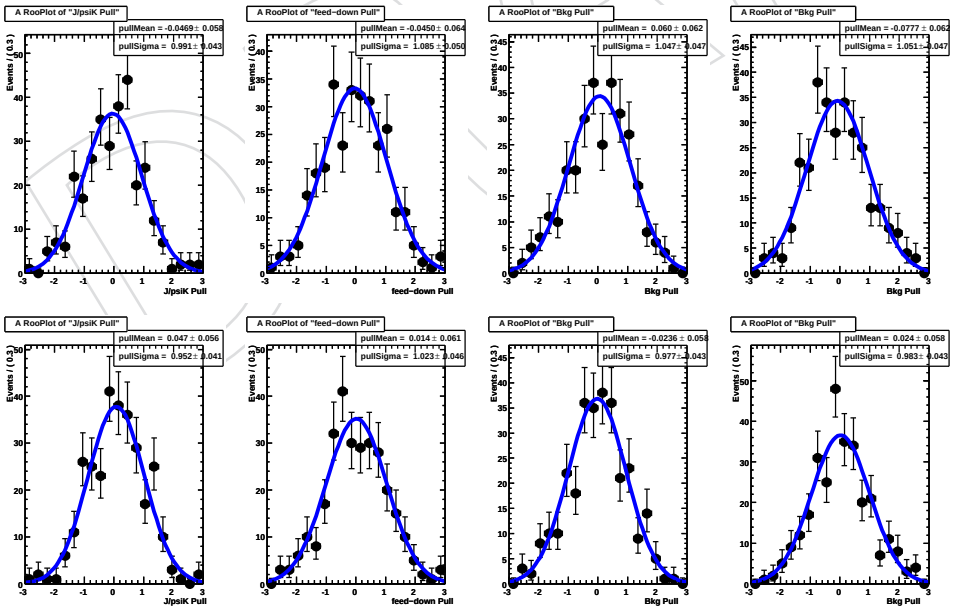

Figure 17: Pull distributions $(n_{\text{fit}} - \langle n \rangle)/\sigma$ for 400 toy experiments simulating the final fit (we do not replicate the sideband fitting procedure in these studies). The top (bottom) row is for p_T^B bin 5–10 (10–13). From left to right within a given row we plot the pull distribution for signal, peaking B (feeddown), non-prompt J/ψ, and prompt J/ψ.

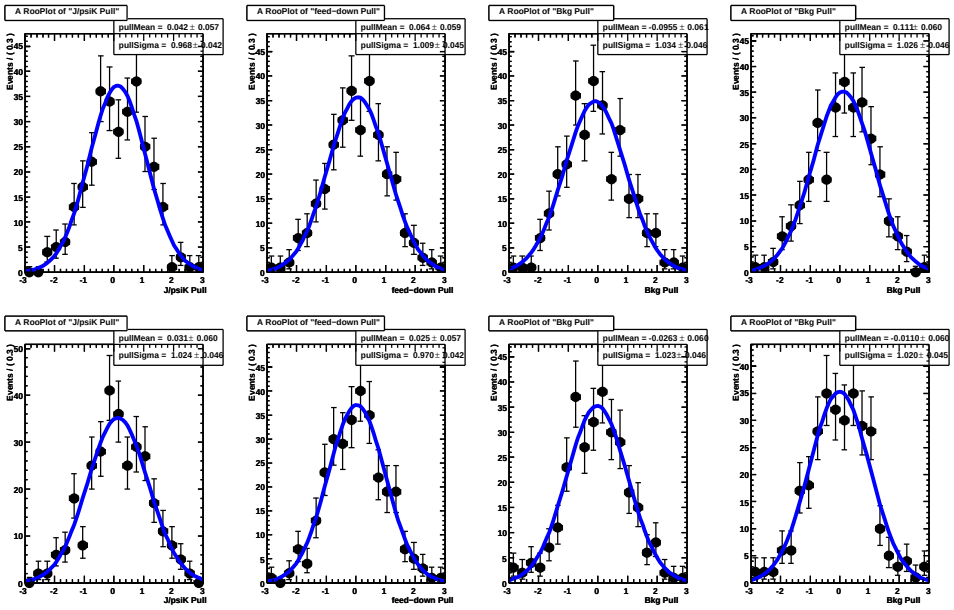

Figure 18: Pull distributions $(n_{\text{fit}} - \langle n \rangle)/\sigma$ for 400 toy experiments simulating the final fit (we do not replicate the sideband fitting procedure in these studies). The top (bottom) row is for p_T^B bin 13–17 (17–24). From left to right within a given row we plot the pull distribution for signal, peaking B (feeddown), non-prompt J/ψ, and prompt J/ψ.

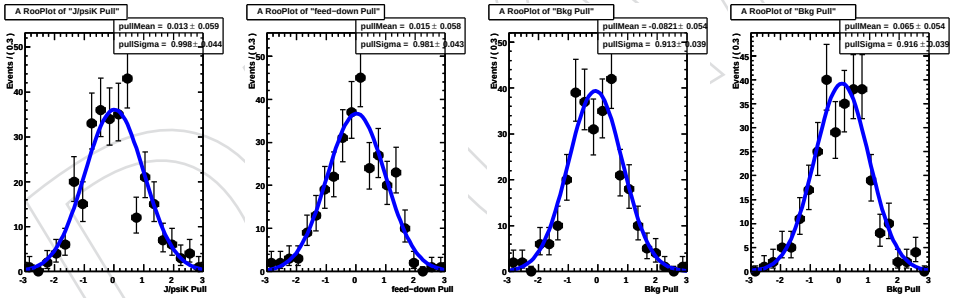

Figure 19: Pull distributions $(n_{\text{fit}} - \langle n \rangle)/\sigma$ for 400 toy experiments simulating the final fit (we do not replicate the sideband fitting procedure in these studies). Results correspond to the $p_T^B > 24\,\text{GeV}/c$ bin. From left to right within a given row we plot the pull distribution for signal, peaking B (feeddown), non-prompt J/ψ, and prompt J/ψ.

Table 12: Summary of number of generated signal events, and pull means and widths for signal yields in each bin of p_T^B from the ensemble of 400 toy experiments in the nominal setup for the B^+ sample.

Bin #	Gen Mean	Pull Mean	Pull Width
1	250	-0.047 ± 0.058	0.991 ± 0.043
2	210	$+0.047 \pm 0.056$	0.952 ± 0.041
3	145	$+0.042 \pm 0.057$	0.968 ± 0.042
4	150	$+0.031 \pm 0.060$	1.024 ± 0.046
5	55	$+0.013 \pm 0.059$	0.998 ± 0.044

Table 13: Summary of signal and background yields determined by fitting simultaneously M_B and ct in bins of p_T^B.

Parameter	Bin 1	Bin 2	Bin 3	Bin 4	Bin 5	Bin 6
N_{sig}	223.1 ± 25.6	235.5 ± 21.1	168.8 ± 17.2	206.6 ± 16.8	56.4 ± 8.8	43.8 ± 7.7
N_{prompt}	16970 ± 301	5387 ± 134	2171 ± 81	842.8 ± 44.8	149.4 ± 19.3	96.7 ± 17.1
$N_{\text{non-prompt}}$	5099 ± 363	1661 ± 161	907.5 ± 97.6	368.2 ± 56.6	52.3 ± 24.7	40.1 ± 23.3
N_{peaking}	140.6 ± 101.0	241.5 ± 54.8	210.5 ± 37.5	109.5 ± 27.0	56.1 ± 13.6	26.2 ± 11.9

expected yields in $3\,\text{pb}^{-1}$. To perform the toy studies we generate events based on the default PDF model, varying the experiment-by-experiment yields based on Poissonian statistics, and then fit using the same model. The pull distributions are defined as $(n_{\text{fit}} - \langle n \rangle)/\sigma$, where n_{fit} and σ are the fitted yield and its error for the given experiment, and $\langle n \rangle$ is the mean of the Poisson distribution for each component (obtained from the values listed in Table 7). We fit each pull distribution to a single Gaussian and report the resulting means and widths in Table 12. We find the expected result, zero mean and unit width, for every component in every bin, thus giving us confidence that the fit machinery corresponding to the nominal setup is performing adequately.

Having established that the nominal fit setup is free of inherent bias, we test for potential bias caused by residual correlations between M_B and ct in signal events by embedding signal MC events into 100 pseudoexperiments. Due to the finite size of the signal and background samples, there is some statistical oversampling in this study. Since this would tend to amplify any real correlations, we consider the results to be a conservative upper limit on potential bias due to correlations between M_B and ct. Figure 20 shows the resulting fitted yield for each bin of p_T^B, which are consistent with the input values (Table 7).

6 Fit Results

In Figs. 21–23 we show the projections of M_B and ct for the full range of $p_T^B > 5\,\text{GeV}/c$, and separately in each of the five p_T^B bins. Table 13 summarizes the yields obtained in each bin of p_T^B, and for reference, Table 14 shows the signal and background yields for the fit over all p_T^B and η^B bins. Figures 26 and 27 show similar fits for each bin in η^B, while Table 16 summarizes the fitted yields and background shape parameters.

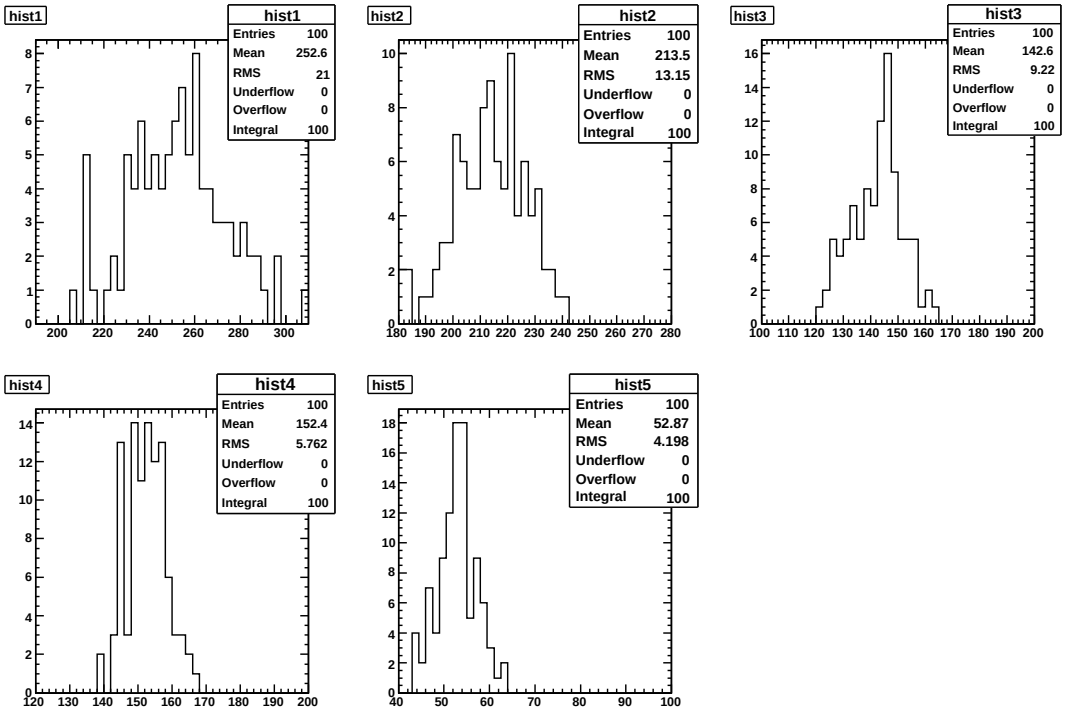

Figure 20: Disributions of fitted signal yields in each of the five bins for the fit B^+ sample, from the embedded toy study described in the text.

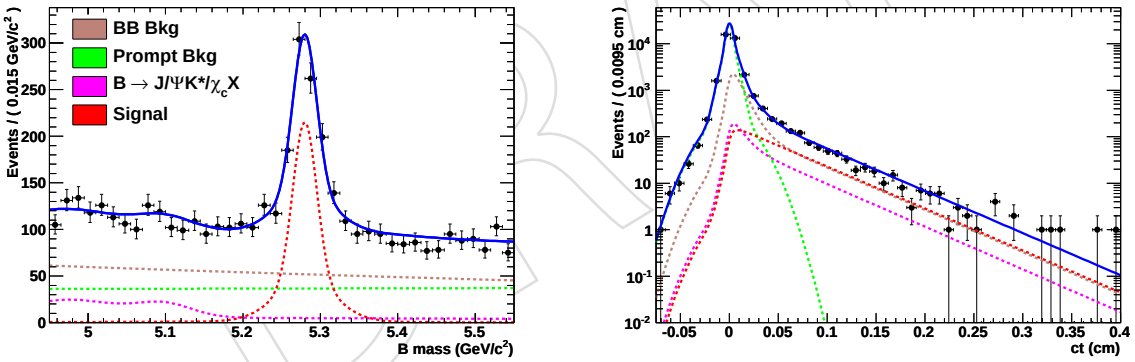

Figure 21: Projections of the fit results in M_B (left) and ct (right) for the full range of $p_T^B > 5\,\text{GeV}/c$. When plotting M_B we require $ct > 100\,\mu\text{m}$ and scale the yields accordingly.

Table 14: Summary of signal and background yields determined by fitting simultaneously M_B and ct for all events satisfying $p_T^B > 5\,\text{GeV}/c$ and $|\eta^B| < 2.4$.

Parameter	$p_T^B > 5\,\text{GeV}/c$
N_{sig}	911.9 ± 46.9
N_{prompt}	28568 ± 224
$N_{\text{non-prompt}}$	5225 ± 234
N_{peaking}	657.1 ± 101.1

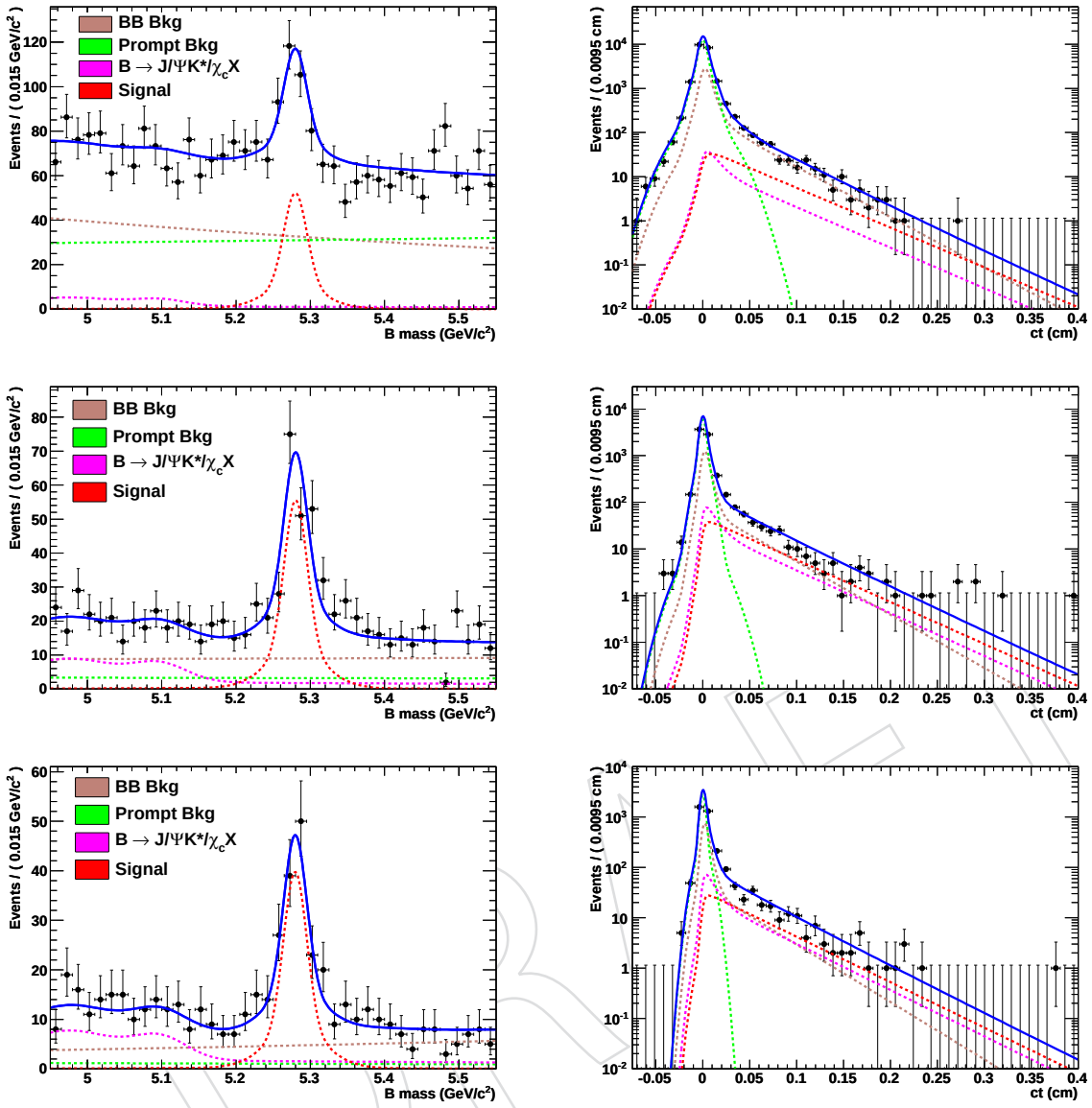

Figure 22: Projections of the fit results in M_B (left) and ct (right) for the B^+ fits for top to bottom (in GeV/c): 5–10, 10–13, 13–17. Individual contributions from the various components are shown in different colors (refer to legend in the M_B plots). When plotting M_B we require $ct > 100\,\mu$m and scale the yields accordingly.

Table 15: Summary of signal and background yields determined by fitting simultaneously M_B and ct in bins of $|y^B|$.

Parameter	Bin 1	Bin 2	Bin 3	Bin 4	Bin 5
N_{sig}	187.3 ± 16.6	163.7 ± 17.0	206.8 ± 20.1	203.0 ± 22.3	175.8 ± 22.3
N_{prompt}	3178 ± 65	3855 ± 74	6231 ± 102	9100 ± 131	6393 ± 111
$N_{\text{non-prompt}}$	574.6 ± 63.3	537.7 ± 71.4	879.0 ± 110.3	1650 ± 150	1231 ± 93
N_{peaking}	111.5 ± 36.1	175.8 ± 38.6	163.7 ± 55.0	196.5 ± 70.6	115 ± 61.4

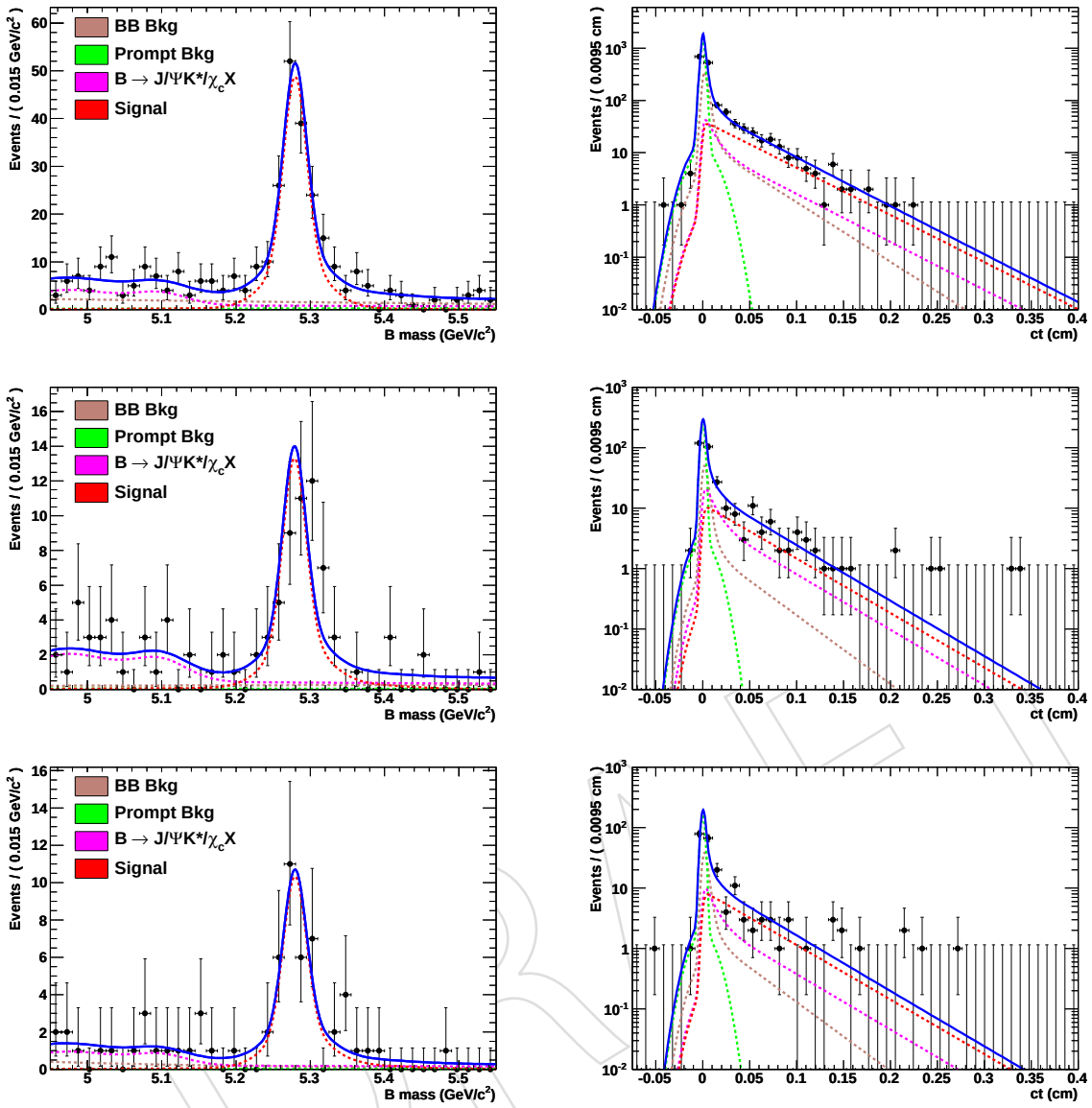

Figure 23: Projections of the fit results in M_B (left) and ct (right) for the B^+ fits for top to bottom (in GeV/c): 17–24, 24–30, and $>$ 30. Individual contributions from the various components are shown in different colors (refer to legend in the M_B plots). When plotting M_B we require $ct > 100\,\mu$m and scale the yields accordingly.

Table 16: Summary of signal and background yields determined by fitting simultaneously M_B and ct in bins of η^B.

Parameter	Bin 1	Bin 2	Bin 3	Bin 4	Bin 5
N_{sig}	165.9 ± 22.3	182.6 ± 18.8	204.7 ± 18.8	196.8 ± 18.6	192.1 ± 21.30
N_{prompt}	7667 ± 118.4	4655 ± 86	3416 ± 69	4747 ± 82	7902 ± 125
$N_{\text{non-prompt}}$	1494 ± 97	890.2 ± 93.4	645.8 ± 70.6	659.7 ± 58.5	853.7 ± 143.4
N_{peaking}	222.3 ± 71.1	170.9 ± 47.6	103.7 ± 38.0	171.8 ± 47.3	225.6 ± 65.7

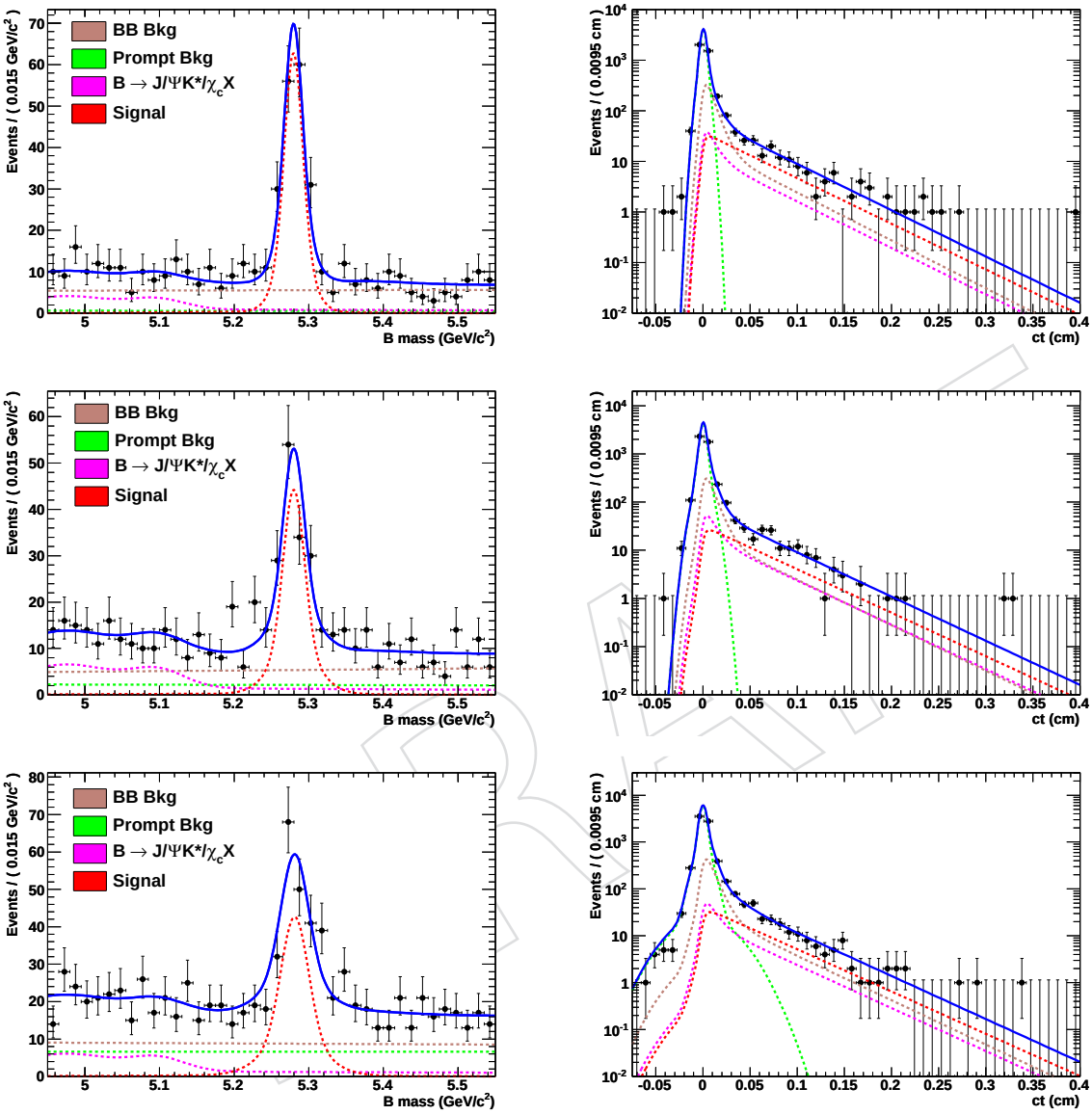

Figure 24: Projections of the fit results in M_B (left) and ct (right) for the B^+ fits for $\left|y^B\right|$ ranges top to bottom: $(0, 0.60)$, $(0.60, 1.10)$, $(1.10, 1.45)$. Individual contributions from the various components are shown in different colors (refer to legend in the M_B plots). When plotting M_B we require $ct > 100\,\mu$m and scale the yields accordingly.

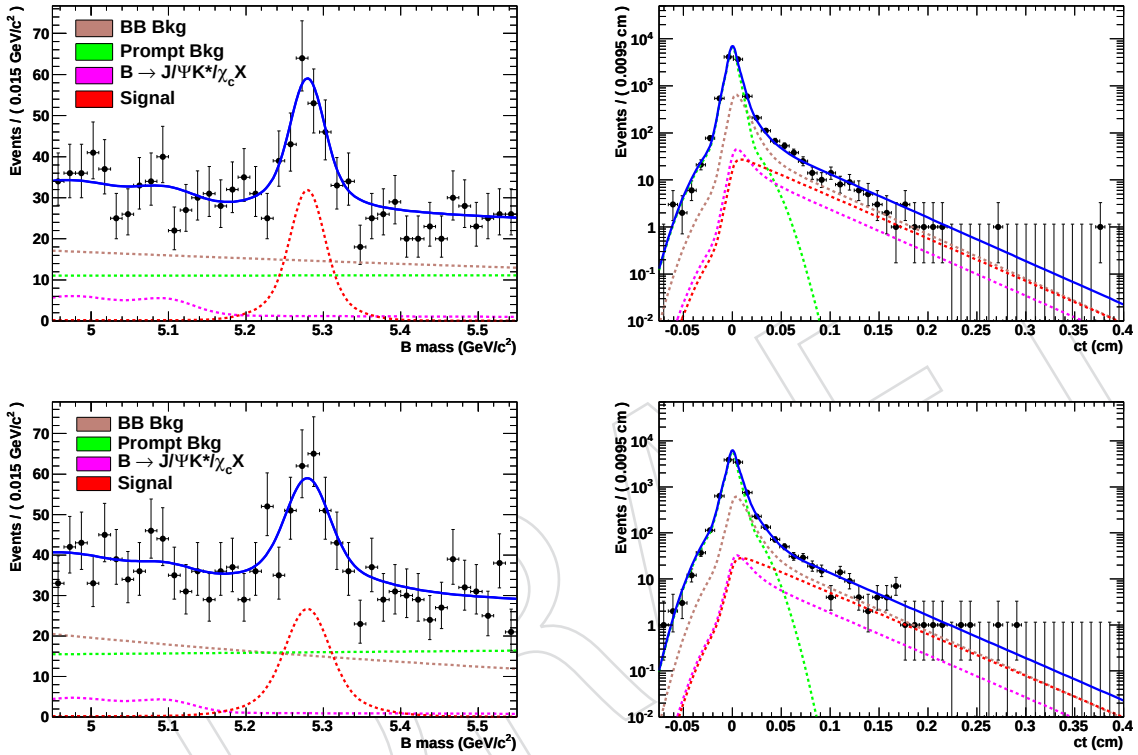

Figure 25: Projections of the fit results in M_B (left) and ct (right) for the B^+ fits for $\left|y^B\right|$ ranges top to bottom: $(1.45, 1.80)$ and $(1.80, 2.40)$. Individual contributions from the various components are shown in different colors (refer to legend in the M_B plots). When plotting M_B we require $ct > 100\,\mu$m and scale the yields accordingly.

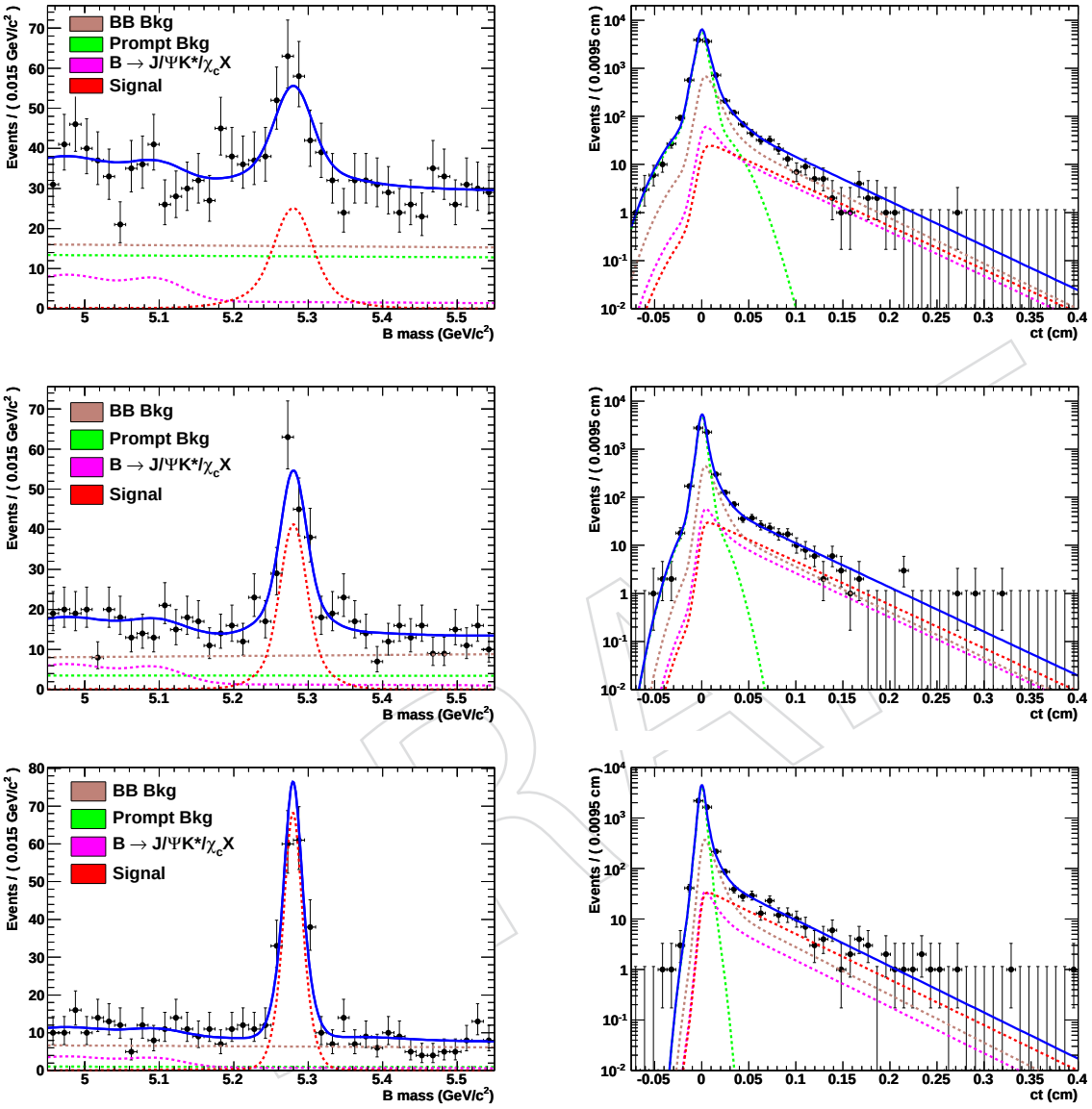

Figure 26: Projections of the fit results in M_B (left) and ct (right) for the B^+ fits for η^B ranges top to bottom: $[-2.4, -1.6]$, $[-1.6, -0.7]$, $[-0.7, +0.7]$. Individual contributions from the various components are shown in different colors (refer to legend in the M_B plots). When plotting M_B we require $ct > 100\,\mu$m and scale the yields accordingly.

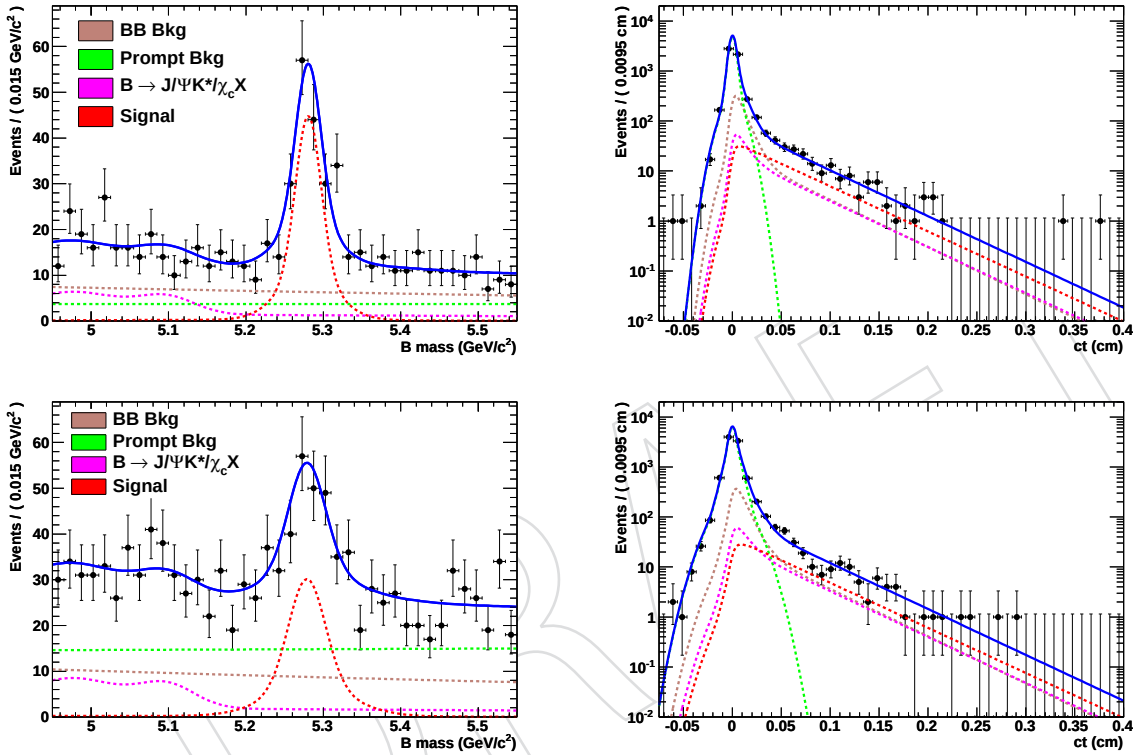

Figure 27: Projections of the fit results in M_B (left) and ct (right) for the B^+ fits for η^B ranges top to bottom: $[+0.7, +1.6]$ and $[+1.6, +2.4]$. Individual contributions from the various components are shown in different colors (refer to legend in the M_B plots). When plotting M_B we require $ct > 100\,\mu$m and scale the yields accordingly.

7 Systematics

We have considered several sources of systematic uncertainty on the cross section measurements. We describe here the various contributions:

- **Branching fractions** – we use the errors on the branching fractions for the $B^{+,0}$ and J/ψ decays as reported in the PDG [1].
- **PDF shapes** – we perform ensembles of fits varying the PDF parameters individually according to their statistical uncertainties. The resulting variation in yields is taken as an estimate of the systematic uncertainty coming from imperfect knowledge of the PDF shapes. Figure 28 illustrates examples of this technique, where we show the distributions of fitted signal yield that results from varying PDF parameters within their uncertainties and refitting. The RMS of a given distribution is the systematic uncertainty on that fit parameter due to variation of the given PDF parameters. We have also considered different assumed functional forms for the PDFs, but the resulting changes in signal yield are less than what we obtain from the PDF parameteric changes. For example, rather than using an exponential to describe the non-peaking background shape in M_B, we tried first- and second-order polynomials. For the peaking B background we tried a single Gaussian (instead of double) plus an exponential, or three Gaussians and no exponential. Finally, for ct we considered a double Gaussian resolution function in place of the default triple Gaussian. In all cases the resulting change in signal yields was 0.5% in the first p_T^B bin, and much less in the other bins. As a final conservative cross-check, we repeat all fits using the shape parameters obtained from MC (Figs. 11 and 12) for **all** PDFs, and we find agreement with our nominal fit yields in all p_T^B (y^B) bins within 5% (10%) relative. This sets an overall scale for the size of the systematic uncertainty that we can expect from imperfect knowledge of the PDFs.
- $\boldsymbol{B^+ \to J/\psi\pi^+}$ – we include a PDF for these events in the nominal fit with the yield fixed according to the rate observed in the simulation. The systematic uncertainty is then evaluated by varying the yield up and down by the error on the measured branching fraction.
- $\boldsymbol{p_T^B}$ **binning** – when computing the differential cross section for B production in a given p_T^B bin we need to correct for the fraction of fitted signal events in the given bin that originate from B mesons generated in a different bin. We take half the correction as a systematic.
- **Trigger/Muon efficiency** – we take the statistical uncertainty from the tag-and-probe procedure in bins of muon p_T and η summed in quadrature with a correlation factor from MC to take into account the assumption that the trigger efficiency is simply the square of the individual efficiencies reported in Table 5.
- **Muon ID** – we take the statistical uncertainty from the tag-and-probe procedure in bins of muon p_T and η propagated to each bin of p_T^B and η^B.
- **Tracking efficiency** – tracking efficiency for muons and hadrons in data has been shown to be consistent with MC predictions with a precision given by the statistical uncertainty from the tag-and-probe procedure for muon efficiency, and 3.9% for hadron efficiency [20].
- **Muon Momentum Scale** – We take the variation in yields when changing the momentum scale correction within its uncertainty.

- **Prob(χ^2)** – The efficiency of this cut on truth-matched signal MC events is 97%, from which we obtain a systematic uncertainty as half the inefficiency. As a cross-check, we fit the data obtained without this cut applied and find deviations from the nominal fit within a few percent.
- **p_T^B spectrum** – We reweight signal MC events according to the difference in the p_T^B spectrum between PYTHIA and MC@NLO and then recalculate all of the efficiencies in the normal way. This is done separately in each bin of p_T^B, $|y^B|$, and η^b. Since the variation in the spectrum is larger for the rapidity bins, which integrate over p_T^B, the corresponding variation in the efficiency calculation is also larger.
- **Decay-in-flight muons** – We find that only 1.1% (0.8%) of the signal events in $B^+ \to J/\psi K^+$ have a hadron associated with a muon segment, and we therefore choose not to veto muons in this analysis. This choice opens the question of the tracking and reconstruction efficiency for signal events where the hadron decays to a muon. Since any study of tracking efficiency for hadrons is susceptible to the same effect, for tracking efficiency we assert that the 3.9% per-track systematic already includes the effect of hadron decays (and also nuclear interactions in the detector, etc). The second effect can be summarized by noting that even if the hadron track exists, the resulting mass of the B candidate could fall outside the fit window due to resolution effects. Figure 29 shows that the reconstructed M_B for $B^+ \to J/\psi K^+$ events where the kaon decays is not much different than the nominal one, giving us some confidence that if the track is reconstructed, the candidates is also reconstructed and passes the nominal selection.
- **B reco** – With the kaon p_T cut at 0.9 GeV/c, we obtain a sample with more than one candidate on average. To check whether this fact has any effect on our final fitted signal yields, we vary the kaon p_T from 0.9 to 1.5 GeV/c and find variations in the fitted signal yields that are less than 4% in all bins. We conclude that there is no strong effect from our choice of kaon p_T threshold. Since we already include a generous systematic uncertainty for hadron tracking efficiency (3.9%), we do not assign an additional systematic uncertainty for the kaon p_T cut.
- **MC statistics** – uncertainty on the reconstruction efficiency due to finite Monte Carlo sample size.
- **Misalignment** – we use two different signal MC samples reconstructed with different assumed alignments and evaluate the systematic uncertainty as the difference in reconstruction efficiency between the two samples. The two samples are:
  - /BpToJPsiMuMu_2MuPEtaFilter_7TeV-pythia6-evtgen/Summer10-START36_V9_S09-v1/GEN-SIM-RECO
  - /BpToJPsiMuMu_2MuPEtaFilter_7TeV-pythia6-evtgen/Summer10-DESIGN_36_V8_S09-v1/GEN-SIM-RECO
- **FSR** – to check for possible systematic effects from a radiative tail in the distribution of M_B, we remove all events in the signal MC sample where `PHOTOS` produced a photon in association with the B^+ decay. We then recompute the signal efficiency, and reparameterize the signal PDF shape in M_B from this new sample and quote the difference in yields as the systematic.
- **Luminosity** – we use an uncertainty of 11% on the luminosity estimate [21].

The resulting systematic uncertainty on the cross section is summarized in Tables 17- 18, where the total systematic in each bin is calculated as the sum in quadrature of the individual uncertainties. The dominant sources of systematics are the luminosity, branching fractions, and efficiencies.

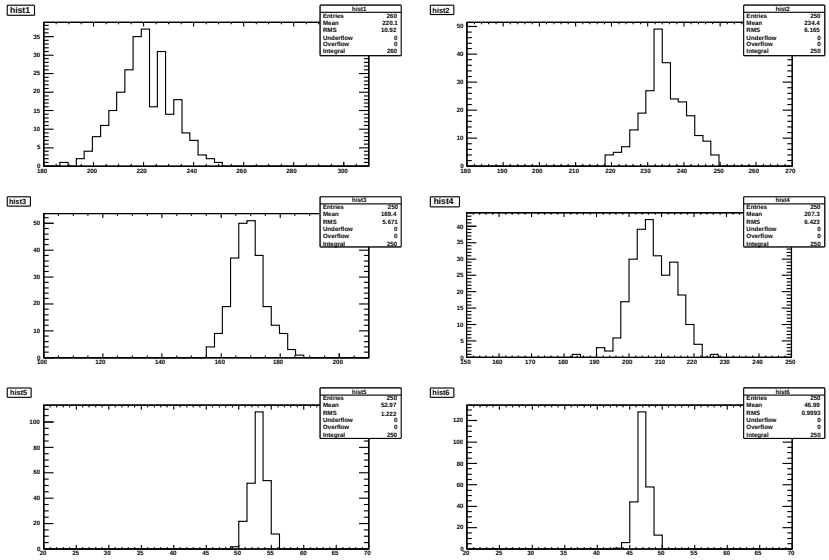

Figure 28: Distributions of fitted signal yield for ensembles of B^+ toy experiments where PDF parameters are varied within their statistical uncertainties. Each plot corresponds to the same PDF parameter being varied, but in different bins of p_T^B (after rotating: top left is the lowest bin, increasing clockwise). The RMS of each distribution is taken as the systematic uncertainty coming from imperfect knowledge of the given parameter.

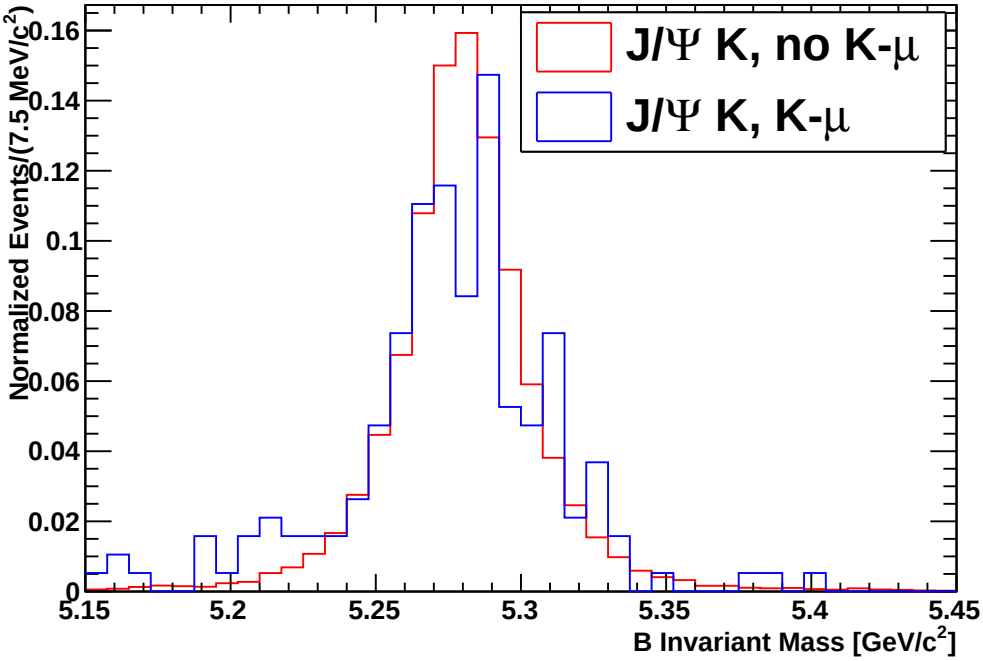

Figure 29: Reconstructed invariant mass for $B^+ \to J/\psi K^+$ events where the kaon does (blue) or does not (red) decay to a muon.

Table 17: Summary of systematic uncertainties (%) on the B^+ cross section in bins of p_T^B. We calculate the total uncertainty as the sum in quadrature of the individual uncertainties, and we show separately the total uncertainty with and without the luminosity included.

Source	Bin 1	Bin 2	Bin 3	Bin 4	Bin 5	Bin 6
Branching fractions	3.5	3.5	3.5	3.5	3.5	3.5
PDF/fit	5.0	2.6	3.3	3.1	2.3	2.1
$B^+ \to J/\psi\pi^+$	0.1	0.1	0.1	0.3	0.2	0.1
Trigger Eff	1.2	1.7	1.3	2.5	3.1	3.0
Muon ID	0.8	0.9	1.0	1.2	1.2	1.1
Muon trk Eff	1.2	0.9	1.0	1.2	1.3	1.1
Hadron trk Eff	3.9	3.9	3.9	3.9	3.9	3.9
Muon Momentum scale	0.6	0.8	0.5	0.9	1.6	1.6
Prob(χ^2)	1.5	1.5	1.5	1.5	1.5	1.5
p_T^B spectrum	1.0	0.5	0.5	0.6	0.7	2.3
ct resolution	1.7	1.5	1.4	1.2	1.0	0.9
p_T binning	1.1	1.8	1.7	1.5	1.9	1.0
MC Statistics (eff)	1.1	1.2	1.2	1.5	3.4	3.9
MC Statistics (flt*acc)	0.6	1.0	1.3	1.8	3.5	4.7
Misalignment	2.3	2.1	1.7	1.6	1.6	2.0
FSR	0.5	0.2	0.3	0.3	1.6	2.0
Non-Luminosity	8.4	7.4	7.5	7.8	9.2	10.0
Luminosity	11	11	11	11	11	11
Total	13.8	13.2	13.3	13.5	14.3	14.9

Table 18: Summary of systematic uncertainties (%) on the B^+ cross section in bins of $|y^B|$. We calculate the total uncertainty as the sum in quadrature of the individual uncertainties, and we show separately the total uncertainty with and without the luminosity included.

Source	Bin 1	Bin 2	Bin 3	Bin 4	Bin 5
Braching Fractions	3.5	3.5	3.5	3.5	3.5
PDF/fit	2.8	3.2	3.5	3.8	3.9
$B^+ \to J/\psi\pi^+$	0.1	0.1	0.1	0.1	0.2
Trigger Eff	1.4	1.8	2.1	2.3	2.3
Muon ID	0.9	1.1	1.2	1.0	0.9
Muon trk Eff	0.9	1.1	1.3	1.3	1.3
Hadron trk Eff	3.9	3.9	3.9	3.9	3.9
Muon Momentum scale	0.5	0.4	0.5	0.6	0.7
Prob(χ^2)	1.5	1.5	1.5	1.5	1.5
p_T^B spectrum	3.9	4.2	4.3	4.4	4.4
ct resolution	0.6	1.1	1.3	1.4	1.4
$\|y^B\|$ binning	0.2	0.2	0.4	0.5	0.4
MC Statistics (eff)	1.8	1.8	1.8	1.5	1.7
MC Statistics (flt*acc)	1.0	0.9	1.1	1.0	1.1
Misalignment	1.6	1.7	2.4	2.5	2.6
FSR	0.2	0.3	0.2	0.4	0.3
Non-Luminosity	8.0	8.5	9.0	9.2	9.3
Luminosity	11	11	11	11	11
Total	13.6	13.9	14.2	14.3	14.4

Table 19: Summary of systematic uncertainties (%) on the B^+ cross section in bins of η^B. We calculate the total uncertainty as the sum in quadrature of the individual uncertainties, and we show separately the total uncertainty with and without the luminosity included.

Source	Bin 1	Bin 2	Bin 3	Bin 4	Bin 5
Braching Fractions	3.5	3.5	3.5	3.5	3.5
PDF/fit	3.6	3.4	2.7	3.1	3.7
$B^+ \to J/\psi\pi^+$	0.1	0.1	0.2	0.1	0.1
Trigger Eff	2.3	2.2	1.8	2.2	2.3
Muon ID	0.8	1.1	0.9	1.1	0.8
Muon trk Eff	1.3	1.1	0.7	1.1	1.3
Hadron trk Eff	3.9	3.9	3.9	3.9	3.9
Muon Momentum scale	0.7	0.7	0.6	0.8	0.7
Prob(χ^2)	1.5	1.5	1.5	1.5	1.5
p_T^B spectrum	4.3	4.0	3.8	4.1	4.2
ct resolution	1.4	1.2	0.5	1.2	1.4
η binning	0.2	0.1	0.1	0.1	0.2
MC Statistics (eff)	1.7	1.7	1.7	1.7	1.7
MC Statistics (flt*acc)	1.0	1.0	1.0	1.0	1.0
Misalignment	2.2	2.1	1.8	2.2	2.3
FSR	0.5	0.2	0.2	0.5	0.3
Non-Luminosity	8.8	8.5	7.8	8.5	8.8
Luminosity	11	11	11	11	11
Total	14.1	13.9	13.0	13.5	14.1

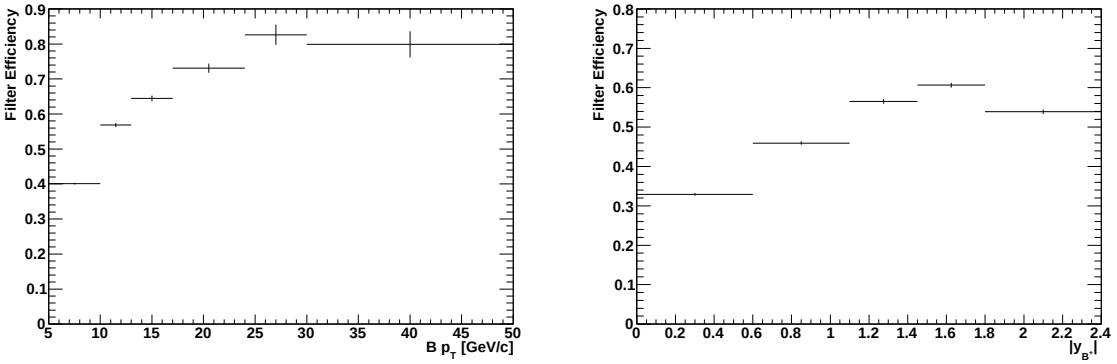

Figure 30: Summary of the filter efficiency times acceptance in each bin of p_T^B (left) and $|y^B|$ (right).

Table 20: Summary of differential cross sections $d\sigma/dp_T^B$ (μb/ GeV/c) in bins of p_T^B. For the data measurements, the uncertainties are statistical, non-luminosity systematic, and the luminosity systematic, respectively. The last bin of p_T^B is unbounded on the upper end, so it is quoted as an integrated cross section σ (in μb) above the p_T^B threshold of 24 GeV/c.

Bin #	$d\sigma/dp_T^B$ (μb/ GeV/c)	MC@NLO	PYTHIA
1	$4.07 \pm 0.47 \pm 0.34 \pm 0.45$	2.73	4.92
2	$1.47 \pm 0.13 \pm 0.11 \pm 0.16$	0.90	2.07
3	$0.412 \pm 0.041 \pm 0.031 \pm 0.045$	0.39	0.81
4	$0.181 \pm 0.015 \pm 0.014 \pm 0.020$	0.12	0.22
5	$0.042 \pm 0.007 \pm 0.004 \pm 0.005$	0.04	0.06
6	$0.188 \pm 0.034 \pm 0.019 \pm 0.021$	0.16	0.20

8 Final Results and Conclusions

We calculate the differential cross section in bins of p_T^B, $|y^B|$, and η^B with the following equations:

$$\frac{d\sigma(pp \to B^+X)}{dp_T^B} = \frac{n_{\rm sig} \cdot f_{\rm bin}}{2 \cdot \epsilon_{\rm filt} \cdot \epsilon_{\rm trig} \cdot \epsilon_{\rm reco} \cdot \mathcal{B}(B^+ \to J/\psi K^+) \cdot \mathcal{B}(J/\psi \to \mu\mu) \cdot \mathcal{L} \cdot \Delta p_T^B}, \quad (5)$$

and similiarly for $|y^B|$ and η^B, where $n_{\rm sig}$ is the fitted number of signal events in the given bin, $f_{\rm bin}$ is the correction factor for bin-to-bin migration, Δp_T^B is the bin size, and the extra factor of 2 accounts for our choice of quoting the B^+ cross sections (rather than $B^\pm$, etc). All efficiencies and the correction factor are calculated separately in each bin. We define the factors for bin-to-bin migration as the fraction of reconstructed and truth-matched candidates in a given bin that were also generated in that bin. The filter efficiencies $\epsilon_{\rm filt}$ is calculated as the fraction of true signal decays generated in a given bin of p_T^B(gen) or $|y^B|$ (gen) that pass the generator-level filter, and are shown in Fig. 30.

The differential cross sections as a function of p_T^B and $|y^B|$ are shown in Figs. 31, and the quantitative results are summarized in Tables 20 and 22. As a cross-check on the forward/backward asymmetry of our measurement, in Fig. 32 we show the measured cross section as a function of η^B. No significant asymmetry is observed.

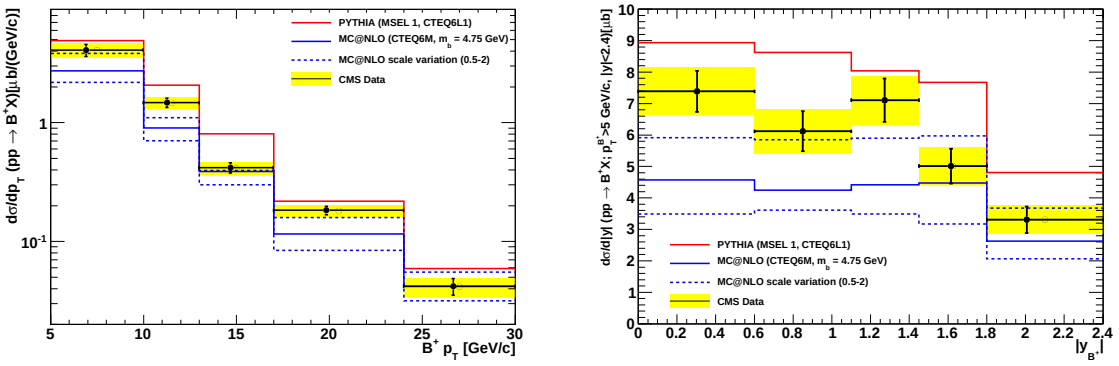

Figure 31: Summary of the measured differential cross section $d\sigma/dp_T^B$ (left) and $d\sigma/d\left|y^B\right|$ (right) compared with the theory predictions.

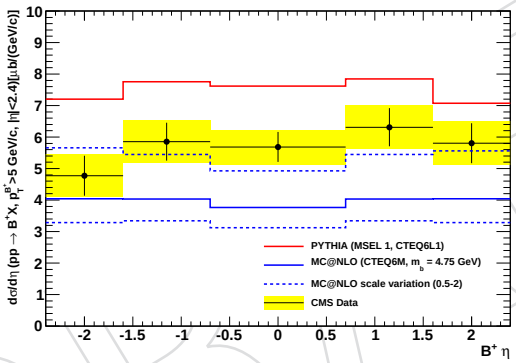

Figure 32: Summary of the measured differential cross section $d\sigma/d\eta^B$ compared with the theory predictions.

Table 21: Summary of B^+ differential cross sections $d\sigma/d\left|y^B\right|$ (μb) in bins of $\left|y^B\right|$. For the data measurements, the uncertainties are statistical, non-luminosity systematic, and the luminosity systematic, respectively.

Bin #	$d\sigma/d\left\|y^B\right\|$ (μb)	MC@NLO	PYTHIA
1	$7.39 \pm 0.65 \pm 0.59 \pm 0.81$	4.6	8.9
2	$6.11 \pm 0.64 \pm 0.52 \pm 0.67$	4.3	8.6
3	$7.11 \pm 0.69 \pm 0.64 \pm 0.78$	4.4	8.0
4	$5.01 \pm 0.55 \pm 0.46 \pm 0.55$	4.5	7.7
5	$3.31 \pm 0.42 \pm 0.31 \pm 0.36$	2.6	4.8

Table 22: Summary of B^+ differential cross sections $d\sigma/d\eta^B$ (μb) in bins of η^B. For the data measurements, the uncertainties are statistical, non-luminosity systematic, and the luminosity systematic, respectively.

Bin #	$d\sigma/d\eta^B$ (μb)	MC@NLO	PYTHIA
1	$4.78 \pm 0.63 \pm 0.43 \pm 0.53$	4.0	7.2
2	$5.85 \pm 0.60 \pm 0.51 \pm 0.64$	4.0	7.8
3	$5.68 \pm 0.48 \pm 0.45 \pm 0.62$	3.8	7.6
4	$6.31 \pm 0.61 \pm 0.54 \pm 0.69$	4.0	7.8
5	$5.81 \pm 0.63 \pm 0.52 \pm 0.64$	4.0	7.1

In summary, we have measured the differential production cross section for B^+ mesons using the decay $B^+ \to J/\psi K^+$. We find that the predictions of PYTHIA and MC@NLO for the shape of the cross section in p_T^B and $|y^B|$ match the data well, while the normalization falls between the predictions of PYTHIA (on the high side) and MC@NLO (on the low side).

References

[1] Particle Data Group Collaboration, "Review of particle physics", *J. Phys.* **G37** (2010) 075021. doi:10.1088/0954-3899/37/7A/075021.

[2] D0 Collaboration, "Measurement of the angular and lifetime parameters of the decays $B_d^0 \to J/\psi K^{*0}$ and $B_s^0 \to J/\psi\phi$", *Phys. Rev. Lett.* **102** (2009) 032001, arXiv:0810.0037. doi:10.1103/PhysRevLett.102.032001.

[3] CDF Collaboration, "Measurement of the B+ production cross section in p anti-p collisions at s**(1/2) = 1960-GeV", *Phys. Rev.* **D75** (2007) 012010, arXiv:hep-ex/0612015. doi:10.1103/PhysRevD.75.012010.

[4] CDF Collaboration, "Measurement of the Λ_b^0 Lifetime in $\Lambda_b^0 \to J/\psi\Lambda^0$ in $p\bar{p}$ Collisions at $\sqrt{s}$ = 1.96-TeV", *Phys. Rev. Lett.* **98** (2007) 122001, arXiv:hep-ex/0609021. doi:10.1103/PhysRevLett.98.122001.

[5] D0 Collaboration, "Measurement of the ratio of B^+ and B^0 meson lifetimes", *Phys. Rev. Lett.* **94** (2005) 182001, arXiv:hep-ex/0410052. doi:10.1103/PhysRevLett.94.182001.

[6] CDF Collaboration, "Measurement of the lifetime difference between B(s) mass eigenstates", *Phys. Rev. Lett.* **94** (2005) 101803, arXiv:hep-ex/0412057. doi:10.1103/PhysRevLett.94.101803.

[7] CDF Collaboration, "A study of $B^0 \to J/\psi K^{(*)0}\pi^+\pi^-$ decays with the Collider Detector at Fermilab", *Phys. Rev. Lett.* **88** (2002) 071801, arXiv:hep-ex/0108022. doi:10.1103/PhysRevLett.88.071801.

[8] CDF Collaboration, "Measurement of the decay amplitudes of $B^0 \to J/\psi K^{*0}$ and $B_s^0 \to J/\psi\phi$ decays", *Phys. Rev. Lett.* **85** (2000) 4668–4673, arXiv:hep-ex/0007034. doi:10.1103/PhysRevLett.85.4668.

[9] BABAR Collaboration, "Measurement of decay amplitudes of $B \to J/\psi K^*$, $\psi(2S)K^*$, and $\chi_{c1}K^*$ with an angular analysis", *Phys. Rev.* **D76** (2007) 031102, arXiv:0704.0522. doi:10.1103/PhysRevD.76.031102.

[10] Belle Collaboration, "Studies of CP violation in B –¿ J/psi K* decays", *Phys. Rev. Lett.* **95** (2005) 091601, arXiv:hep-ex/0504030. doi:10.1103/PhysRevLett.95.091601.

[11] BABAR Collaboration, "Study of $B^\pm \to J/\psi\pi^\pm$ and $B^\pm \to J/\psi K^\pm$ decays: Measurement of the ratio of branching fractions and search for direct CP violation", *Phys. Rev. Lett.* **92** (2004) 241802, arXiv:hep-ex/0401035. doi:10.1103/PhysRevLett.92.241802.

[12] H.-U. Bengtsson and T. Sjostrand, "The Lund Monte Carlo for Hadronic Processes: Pythia Version 4.8", *Comput. Phys. Commun.* **46** (1987) 43. doi:10.1016/0010-4655(87)90036-1.

[13] D. J. Lange, "The EvtGen particle decay simulation package", *Nucl. Instrum. Meth.* **A462** (2001) 152–155. doi:10.1016/S0168-9002(01)00089-4.

[14] M. Mulders et al., "Muon Identification in CMS", *CMS Note AN-2008-098* , **http://cms.cern.ch/iCMS/jsp/openfile.jsp?tp=draft&files=AN2008_098_v1.pdf** (2008).

[15] CMS Collaboration , *CMS Physics Analysis Summary BPH-09-001* , (2010).

[16] CMS Collaboration , *CMS Physics Analysis Summary BPH-10-003* , **http://cms.cern.ch/iCMS/analysisadmin/get?analysis=BPH-10-003-paper-v1.pdf** (2010).

[17] N. Adam et al., "Measurement of the Inclusive Upsilon Production Cross section in pp Collisions at $\sqrt{s} = 7$ TeV", *CMS Note AN-10-140* , **http://cms.cern.ch/iCMS/jsp/openfile.jsp?tp=draft&files=AN2010_140_v2.pdf** (2010).

[18] T. Speer, "Offline Primary Vertex Finding", *CMS Twiki page* , **https://twiki.cern.ch/twiki/bin/view/CMS/WorkBookOfflinePrimaryVertexFinding** (2008).

[19] D. L. Pegna and J. Olsen *CMS Note AN-09-079* , **http://cms.cern.ch/iCMS/jsp/openfile.jsp?tp=draft&files=AN2007_009_v2.pdf** (2007).

[20] CMS Collaboration , *CMS Physics Analysis Summary TRK-10-002* , (2010).

[21] CMS Collaboration , *CMS Physics Analysis Summary TRK-10-002* , (2010).